Title

Catecholaminergic axon innervation and morphology in flat-mounts of atria and ventricles of mice.

Journal

The Journal of Comparative Neurology, 531(5)

Authors

Bizanti, Ariege
Zhang, Yuanyuan
Harden, Scott
et al.

Publication Date

2023-04-01

DOI

10.1002/cne.25444

Published in final edited form as:
J Comp Neurol. 2023 April ; 531(5): 596–617. doi:10.1002/cne.25444.

Catecholaminergic Axon Innervation and Morphology in Flat-mounts of Atria and Ventricles of Mice

Ariege Bizanti[1,#], **Yuanyuan Zhang**[1,#], **Scott W. Harden**[1,#], **Jin Chen**[1], **Donald B. Hoover**[2], **David Gozal**[3], **Kalyanam Shivkumar**[4], **Zixi Jack Cheng**[1]

[1]Burnett School of Biomedical Sciences, College of Medicine, University of Central Florida, Orlando, FL 32816

[2]Department of Biomedical Sciences, Quillen College of Medicine, East Tennessee State University, Johnson City, TN 37614

[3]Department of Child Health and Child Health Research Institute, and Department of Medical Pharmacology and Physiology, University of Missouri School of Medicine, Columbia, MO 65201

[4]Department of Medicine, Cardiac Arrhythmia Center and Neurocardiology Research Program of Excellence, University of California, Los Angeles, CA 90095.

Abstract

Sympathetic efferent axons regulate cardiac functions. However, the topographical distribution and morphology of cardiac sympathetic efferent axons remain insufficiently characterized due to the technical challenges involved in immunohistochemical labeling of the thick walls of the whole heart. In this study, flat-mounts of the left and right atria and ventricles of FVB mice were immunolabeled for tyrosine hydroxylase (TH), a marker of sympathetic nerves. Then, the atrial and ventricular flat-mounts were scanned using a confocal microscope, and 3D-montages were constructed. We found: 1) *In* the *left and right atria:* A few large TH-immunoreactive (IR) axon bundles entered both atria, branched into small bundles and then single axons that eventually formed very dense terminal networks in the epicardium and myocardium, as well as in the inlet regions of great vessels to the atria. TH-IR varicose axons had close contact with cardiac muscle fibers, vessels, and adipocytes. Multiple intrinsic cardiac ganglia (ICG) were identified in the epicardium of both atria. A subpopulation of principal neurons (PNs) in ICG was TH-IR. Most TH-IR axons in bundles traveled through ICG before forming dense varicose terminal networks in the epicardium and myocardium. However, we did not observe TH-IR axons forming varicose terminals in close approximation or encircling ICG neurons. Small intensely fluorescent (SIF) cells were also found among the ICG, and they were strongly TH-IR. 2) *In the left and*

Correspondence to: Zixi (Jack) Cheng, Ph.D., Burnett School of Biomedical Sciences, College of Medicine, University of Central Florida, 4110 Libra Drive, Orlando, FL 32816. Tel: (407) 823 1505, Fax: (407) 823 0956, zixi.cheng@ucf.edu.

[#]These authors contributed equally

Authors' Contribution

Z.J.C. designed and supervised the study. A.B., S.H. and Z.J.C. wrote the manuscript. S.H. prepared and processed the tissues with immunohistochemistry and scanned using confocal. S.H, A.B. and Y.Z. analyzed data as well as prepared images and microphotographs. A.B., Y.Z., S.H., J.C., and Z.J.C. interpreted data. D.H., D.G., and K.S. provided valuable insights and expertise and helped interpreting the data. All authors edited the manuscript, contributed important intellectual content, and approved its final version.

Conflict of Interest Statement

The authors declare that there is no conflict of interest.

right ventricles and interventricular septum: TH-IR axons entered the ventricles and formed very dense terminal networks in the epicardium and myocardium as well as along the vasculature. Collectively, TH labeling is readily achievable in flat-mounts of thick atrial and ventricular walls, which enabled detailed mapping of catecholaminergic axons and terminal structures in the whole heart at the single cell/axon/varicosity scale. This approach provides a foundation for future quantitative analysis of the topographical organization of the cardiac sympathetic innervation of the whole atria and ventricles under different physiological and pathological conditions.

Graphical Abstract

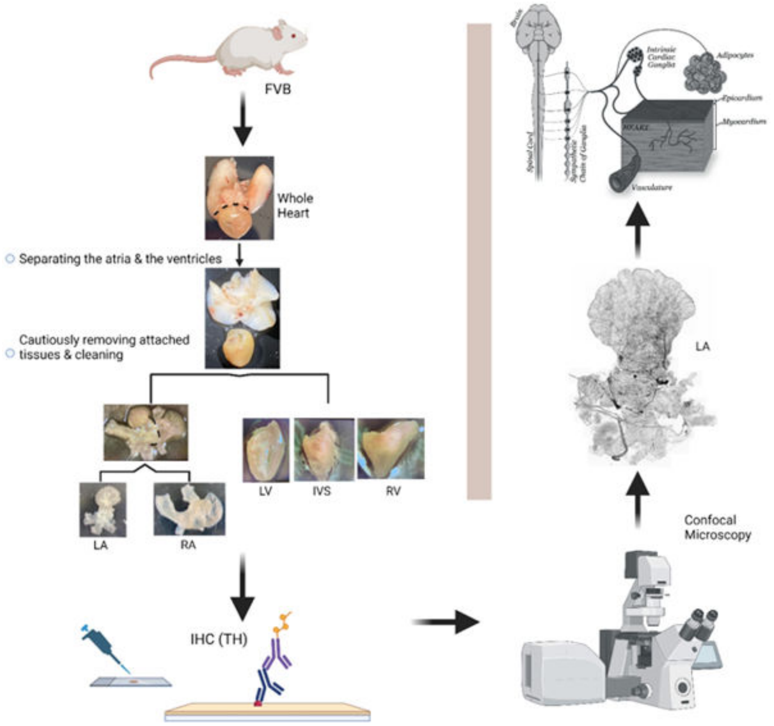

Keywords

Tyrosine hydroxylase; Sympathetic efferent; Intrinsic cardiac nervous system; Cardiac ganglia; Heart; Atria; Ventricles

1. Introduction

Cardiac functions are modulated through sympathetic and parasympathetic (vagal) innervation of the heart. Previously, we examined vagal afferent and efferent innervation of the normal heart and their anatomical remodeling and functional changes in disease models of rats and mice (Ai et al., 2007a; Ai et al., 2007b; Chen et al., 2021; Cheng and Powley, 2000; Cheng et al., 1999; Cheng et al., 2004; Gu et al., 2008; Lin et al., 2008; Yan et al., 2009; Yan et al., 2008). In addition, we studied the distribution and morphology of nociceptive calcitonin gene-related peptide (CGRP-IR) and substance P (SP-IR) afferent axons in the mouse atria (Li et al., 2014). However, the comprehensive topographical mapping of sympathetic innervation of the heart (atria and ventricles) remains only partially documented. Traditionally, intrinsic cardiac ganglia (ICG) were considered as a parasympathetic relay station, and earlier studies claimed that ICG contained only postganglionic parasympathetic neurons that provided cholinergic innervation to the heart (Armour, 1999). More recently, it was demonstrated that the intrinsic cardiac nervous system, which includes a very complex ICG network, is considered as a little heart brain that integrates inputs from multiple sources and comprises sensory, interconnecting, sympathetic and parasympathetic neurons (Ardell et al., 2016; Armour, 2008; Hanna et al., 2021; Parsons, 2004; Shivkumar et al., 2016). Despite the growing interest in ICG composition and function, phenotypic and morphological characterization of ICG neurons is still lacking (Fedele and Brand, 2020; Herring and Paterson, 2021).

Tyrosine hydroxylase (TH) has been widely used as a marker for the sympathetic innervation of the heart (Hanna et al., 2021; Hanna et al., 2017; Rajendran et al., 2019). Most previous studies used thin sections of the heart (atria and ventricles) or partial whole-mounts (or equally flat-mounts as used in the present paper) of the atria in several different species including mice, rats, guinea pigs, pigs, and humans (Ajijola et al., 2015; Calupca et al., 2001; Hoover et al., 2009; Richardson et al., 2003). Though these studies showed innervation by TH-IR axons in cardiac muscles, conducting systems, and/or ICG, sectioning of the cardiac tissues removed the continuity of axons and terminal structures, leading to a partial or incomplete view of the sympathetic innervation of the heart. Although flat-mount atrial tissues were also used in mice and rats, these studies mainly focused on some special cardiac targets, such as the chemical coding of axons within cardiac ganglia and the conduction system (Parsons, 2004; Richardson et al., 2003), and could not provide a complete picture of the sympathetic innervation pattern and morphology in the whole heart, including the atria, ventricles and interventricular septum (IVS). Some studies assessed the distribution of cholinergic and adrenergic nerve fibers in the flat-mount atrial preparations in different species (Inokaitis et al., 2016; Pauza et al., 2014; Pauza et al., 2013; Rysevaite et al., 2011). However, thick regions of the atria (e.g., auricles) and other structures (e.g., superior vena cava, inferior vena cava, pulmonary veins) were removed. Moreover, only larger bundles of nerves were observed in these atrial and ventricular preparations and small regions had to be selected to reveal the fine details of TH-IR axon innervation. Mapping of noradrenergic nerves in the atria and ventricles at the whole organ scale and in high resolution was not available. Recently, tissue-clearing techniques enabled better visualization of the innervation of the whole heart in 3D (Rajendran et al., 2019). However, the visualization of fine axons and terminals in cleared hearts is still limited. Moreover, tissue clearing reduces the ability to visualize other cardiac targets such as ganglion cells, muscles, blood vessels, and adipocytes. Thus, higher-resolution imaging is needed to reveal the intricate patterns of TH-IR axons and their terminal networks in the atrial and ventricular targets.

Here, we aimed to develop tissue processing and imaging methods capable of providing a more complete and comprehensive view of the TH-IR nerves and terminal processes in the mouse heart. After immunolabeling of TH in flat-mounts of the whole atria and large partial ventricles, high-resolution images were acquired that allowed the visualization of delicate TH-IR axons and terminals. We also aimed to assess whether TH-IR axons substantially innervate ICG in mice. To this end, we used immunofluorescence to label TH in the flat-mounts of the whole right and left atria (RA and LA) and right and left ventricles as well as the IVS and scanned them using a confocal microscope with high resolution, after which the distribution and morphology of TH-IR axons and terminals were surveyed at the single cell/axon/varicosity scale.

2. Materials and Methods

2.1 Animals

Male FVB mice (n = 6, age 3–6 months; Jax 001800) were used for this study because they have been widely used for transgenic studies as well as serving as wild-type controls in our previous work investigating cardiac neuroanatomy in the context of various pathologies (Gu et al., 2008, 2009; Li et al., 2010; Lin et al., 2010, 2011; Yan et al., 2009). All animals were housed in a room in which light/dark cycles were set to 12 h/12 h (6:00 AM to 6:00 PM light cycle) and provided food and water *ad libitum*. All procedures were approved by the University of Central Florida Animal Care and Use Committee and strictly followed the guidelines established by the NIH. All experiments conformed to the University of Central Florida guidelines on the ethical use of animals.

2.2 Tissue preparation

Mice were anesthetized with a lethal dose of sodium pentobarbital (i.p., 100 μg/g). Sufficient depth of anesthesia was determined by the complete absence of the hind paw pinch withdrawal reflex. Mice were perfused through the left ventricle with 37 °C phosphate-buffered saline (0.1 M PBS, pH=7.4). The inferior vena cava was cut to drain the blood and perfusate. Tissues were then fixed by perfusion with 4 °C Zamboni's fixative (15% picric acid and 2% paraformaldehyde in PBS, pH=7.4). The heart and lungs were removed together with the trachea and the esophagus to ensure the inclusion of all cardiac tissues. These specimens were postfixed in 4 °C Zamboni's fixative for at least 24 h.

The heart and lungs were separated following fixation. Briefly, the pulmonary veins which attached to the left atrium were separated from the lungs with fine tweezers (Ai et al., 2007a; Cheng, 2017; Cheng et al., 1997a; Li et al., 2010). The atria were then separated from the ventricles (Fig. 1B), and the aortic arch and pulmonary arteries were removed from the atria. The RA and LA were then separated, producing a right atrium with the great vessels, including inferior vena cava (IVC), superior vena cava (SVC), and left precaval vein (LPCV) attached (Fig. 1E), and the left atrium with short segments of all pulmonary veins (PVs) attached (Fig. 1D). The ventricles were further dissected by separating the left ventricle (LV) and right ventricle (RV) from the IVS (Fig. 1F–H) and the LV was trimmed in order to flatten. Tissues were stored in 4 °C PBS until immunohistochemical labeling was initiated.

2.3 Immunohistochemistry

Immunohistochemical procedures were performed on an orbital shaker at room temperature, with each piece of tissue immersed in 0.5–1 mL of reaction liquid in its own chamber of a light-protected 24-well plate. Following tissue preparation, residual Zamboni's fixative was removed from the tissues with 5×10 min washes in PBS. Tissues were then immersed for 5 days (for atria) or 7 days (for ventricles) in a blocking reagent (2% bovine serum albumin, 10% normal donkey serum, 10% normal goat serum, 2% Triton X-100, 0.08% NaN_3 in 0.1 M PBS, pH=7.4) to reduce nonspecific binding of the primary antibody and to promote increased antibody penetration. Primary antibodies (6 μL/mL) were added to the primary solution (2% bovine serum albumin, 4% normal donkey serum, 4% normal goat serum, 0.5% Triton X-100, 0.08% NaN_3 in 0.1 M PBS, pH=7.4) and tissues were incubated for 5 days (for atria) or 7 days (for ventricles). Unbound primary antibodies were removed from tissues by 6×5 min washes with PBST (0.5% Triton X-100 in 0.1 M PBS, pH=7.4). Secondary antibodies (12 μL/mL in PBST) were then applied for 3 days (for atria) or5 days (for ventricles). Unbound secondary antibodies were removed from tissues by 6×5 min washes in PBS. A list of the antibodies used in this study is summarized in Table 1. Tissues were then mounted with their endocardium surface down onto glass slides, crushed with lead weights for 2 days for the atria and 3 weeks for the ventricles, and air-dried under a fume hood. Slides were dehydrated by immersion for 2 min in each of 4 ascending concentrations of ethanol (75%, 95%, 100%, 100%), followed by 2×10 min washes in 100% xylene. Slides were then coverslipped with DEPEX mounting medium (Electron Microscopy Sciences #13514) and allowed to dry overnight. Atrial and ventricular preparations in which primary antibodies were omitted presented no labeling, confirming that nonspecific binding of primary antibodies did not occur.

2.4 Data collection and analysis

Slides were examined using Leica TCS SP5 laser scanning confocal microscope with a HeNe laser to image Alexa Fluor 594-labeled TH in the flat-mounts of the atria and ventricles. An argon–krypton laser (488 nm) was used to detect background autofluorescence of the tissues (e.g., cardiac muscles, ganglionic cells, and blood vessels). For a broad view of the distribution of axons and terminals, tissues were scanned using a 20X oil immersion objective lens (zoom ×1, z-step 1.5 μm), and confocal maximal projection images were generated. To show detailed TH axons and terminals in different layers of the heart, confocal optical sections were scanned using a 40× oil immersion objective lens (zoom 1.5X). The epicardium layer was identified as the outermost layer along with elastic connective and fat tissues, whereas the end of the epicardium and the beginning of the myocardium was identified by the presence of dense muscle fibers in different directions. All confocal images were scanned with similar settings. Modifications, including brightness and contrast adjustments, cropping and scale bar additions, were conducted using Photoshop or NIH ImageJ (Collins 2007) software. Individual scans of a small image window were first obtained by confocal microscopy and saved in stacks of optical section images. Then, these stacks were maximally projected to yield a series of all-in-focus maximum projection tiles (a total of 172 for RA and 119 for LA). MosaicJ (Thévenaz and Unser, 2007) was utilized to align tiles to create large montage images. Counting TH-IR neurons in the ICG was performed using image J cell-counter plugin J. TH and autofluorescent (AF) channels were separated and neurons in each image were counted.

3. Results

3.1 Distribution and morphology of TH-IR axons and terminals in the flat-mount of the whole atria: an overview.

The flat-mounts of the whole right and left atria were prepared (Fig. 1) and TH-IR axon innervation in the right and left atria (RA and LA) was examined (Fig. 2 and Fig. 3). As shown previously (Ai et al., 2009; Lin et al., 2008), multiple intrinsic cardiac ganglia (ICG) were found on the epicardium of the atria. Numerous ICG of different sizes could be found in each of the atria, there were two to three large ganglia in similar locations (SA and AV neuronal complexes) across animals (Ai et al., 2007a; Lin et al., 2008). Although variations in structural details were observed across animals, the general scheme of TH-IR nerves and ICG distribution was similar in all 6 animals studied. In both atria, extrinsic large bundles of TH-IR axons entered the atria. (Figs. 2a and 3a show the right and left atria in a representative mouse. Figs. 2a’ and 3a’ are schematic drawings based on images collected from this representative mouse showing the TH-IR nerve and ICG distributions. As shown in Figs. 2,3, the large axon bundles entered the right atrium along the superior vena cava and left precaval vein, and the left atrium at the entrance region of the pulmonary veins.

These large axon bundles were observed to course through ICG and branched out into smaller bundles multiple times, and finally into individual fine axons, which formed extensive terminal endings over the entire atria including the auricles and the entrance areas of the major veins. Most ICG were observed on the dorsal surface of the LA, specifically around the LA-PV junction (dotted line in LA on (Fig. 3a’). Future density quantification based on the axon number is needed to gain more information on regional density innervation. Also, a more organized pattern of TH-IR axons was seen around the PVs.

3.2 TH-IR axons and terminals innervating epicardial and myocardial layers of the atrial wall

To expose the cardiac targets, we used the 488-nm laser to excite the autofluorescence with red pseudo-color, while using the HeNe laser to excite TH-IR axons with green pseudo-color. TH-IR axon terminals were mostly present in the epicardium (Fig. 4) and the myocardium (Fig. 5) layers. The auricles of the atria contained an abundant and complex network of TH-IR axons, as seen in the higher magnification confocal projection images (Fig. 4, Fig.5). It was generally observed that very rich innervation of TH-IR axons was present at the sinoatrial node (SA) region in the RA and the medial side of LA (Fig. 2a,3a) Additionally, rich innervation was also observed at the center, and the edge of the auricle (Fig. 4b,c and 4b’,c’) as well as the mid-atrium (Fig. 4d,4d’). Details of the terminal morphology of the TH-IR axon network in the auricles were assessed via single optical sections. We identified free terminals at different levels of the myocardium, and the terminating point (terminal ending) was determined as the last varicosity on the axon with an enlarged radius compared to the preceding varicosities. Large bifurcating TH-IR bundles in the epicardium formed a continuous network of varicose axon terminals in the single optical section (Fig. 6a). Such bundles were also observed projecting axons deep into the myocardium (identified by the presence of dense muscle fibers) which formed large, complicated, 3-D terminal endings whose structure could not be entirely captured by a single confocal optical section (Fig. 5a–f, Fig. 6b). In single optical sections, the fragmentary varicose axons formed close contact with the myocytes within the thick myocardium.

3.3 TH-IR neurons in the ICG

As previously reported, multiple ICG of different sizes (large, medium, and small) (Ai et al., 2007a; Lin et al., 2008) were identified in the dorsal surface of the right and left atria (Figs. 2a,3a). Though the total number of ICG may somewhat vary, two large ganglia were consistently found in the same regions of different mice. One of them was located near the SA node region and the other was located near the AV node region (Ai et al., 2007a; Lin et al., 2008). Fig. 7 is an enlarged portion of the middle left atrium and showed 10 ICG including 2 large, 5 medium, and 3 small clusters where some principal neurons (PNs) were TH-IR, and large and small axon bundles traveled through or between these ICG.

To elucidate the structure of ICG and their interaction with catecholaminergic nerve bundles, various ICG are presented as single confocal optical sections (Fig. 8). Consistent with previous reports (Birand, 2008; Pauza et al., 2014; Hoard et al., 2008), a subpopulation of ICG neurons exhibits strong TH-IR (Fig. 8a_{1-3}). However, not all TH-IR ICG PNs expressed the same degree of TH-IR.

Although a subpopulation of ICG TH-IR neurons exhibited strong TH-IR (Fig. 8a, short arrow), some ICG PNs demonstrated weak TH-IR (Fig. 8a, long arrow). Specifically, TH-IR neurons comprised approximately 28.5% ± 3 of all ICG neurons. Interestingly, we identified a ganglion that was located in the rostral SVC and showed more TH-IR neurons relative to non-TH-IR (Fig. 8e).

3.4 Most TH-IR axons branching from extrinsic TH-IR bundles passed by ICG without close contacts with PNs

Numerous TH-IR nerve bundles and axons were observed in ICG. It appeared that their axons mainly coursed through or passed by ganglia (Fig. 8c and 8d) without forming dense varicose endings (putative synaptic contacts) around individual ICG PNs. In contrast, the parasympathetic vagal axons form very dense basket-like endings around ICG PNs (Ai et al., 2009; Li et al., 2010; Lin et al., 2008; Hoard et al., 2008; Brown et al., 2018). TH-IR axons were not observed to directly innervate PNs. However, some delicate varicose axons might have contact with both TH-IR and non-TH-IR PNs (Fig 8c and 8d). Those varicose axons could be projecting from the TH-IR neurons in the ICG. Thus, the majority of postganglionic catecholaminergic axons (Fig. 7) appeared to pass through ICG rather than directly interact with their PNs (Fig. 9a_1–a_2). This sharply contrasted with the catecholaminergic nerve innervation of the gastrointestinal tract where TH-IR axons make numerous synaptic-like varicose endings around many myenteric ganglionic neurons in the stomach and small intestine (Fig. 9b,c, arrowheads), which is consistent with previous reports (Hibberd et al., 2020; Parker et al., 2022; Powley et al., 2016).

3.5 TH-IR Small Intensely Fluorescent (SIF) cells

Small intensely fluorescent (SIF) cells were commonly observed in the atria. SIF cells were identified by their small size (< 10 μm in diameter vs > 20 μm of PNs) and were strongly TH-IR relative to TH-IR PNs (Fig. 10). We frequently observed clusters of SIF cells adjacent to large TH-IR nerve bundles (Fig. 10c) and ICG PNs (Fig. 10a, 10a’,10b, and 10d). Similar to the TH-IR PNs, large and small TH-IR axon bundles traveled through or between clusters of SIF cells without apparent innervation.

3.6 TH-IR axon innervation of vasculature and adipose tissue

TH-IR axons in the atria did not exclusively innervate the muscle. The vasculature was also a common target of TH-IR axons in both right and left atria. Vessels were recognized by a difference in texture and shape compared to surrounding tissues. Vascular structures were often heavily innervated by TH-IR axons: they either wrapped around the structure and/or ran along the blood vessels (Fig. 11a). Adipocytes near the atria were identified by their characteristic round shape, small size, and unique autofluorescence profile (opaque edges with clear centers). Varicose TH-IR axons were observed innervating adipose tissue and forming varicose arborizations around individual adipocytes (Fig. 11b), often forming dense terminal networks from individual axons

3.7 Distribution and morphology of TH-IR axons and terminals in the flat-mount ventricles

Extrinsic large bundles of TH-IR axons entered the RV, LV, and IVS (Figs. 12, 13, 14). These bundles branched out and densely innervated right and left ventricles and IVS with numerous varicose axons. These TH-IR axons traveled from the base of the ventricles and IVS towards the apex with a higher density of axons observed at the basal level. The size of the large TH-IR bundles decreased in size as they bifurcated and descended towards the apex. Blood vessels could be visualized by the well-defined contour within the ventricles (Figs. 12, 13, 14). TH-IR bundles were predominantly present in the epicardium (Fig. 15 a,c,e). Single optical sections revealed the TH-IR axon innervation of the myocardium (Fig. 15 b,d,f). Similar to the atria, long varicose TH-IR axons were present in the myocardium where they traveled in close apposition to myocytes. Only axon fragments could be seen in a single optical section as they did not all exist in a single optical plane, but rather they ran up and down within the thick muscle layer. We were able to visualize axons through the entire wall of the flat-mount ventricles preparations (through all z-stack). Moreover, TH-IR axons ran in parallel with and often wrapped around the blood vessels. The RV had the most apparent vasculature network, but the thickness of LV and partial preparation could contribute to the less apparent vasculature. This was further supported in a parallel study where selected partial projections of the LV that included only a few z-stacks showed a better visualization of the vasculature.

4. Discussion

In the present study, we characterized the distribution and morphology of TH-IR axons and terminals in the flat-mounts of the heart at the single cell/axon/varicosity scale. In the right and left atria, we found extensive networks of TH-IR axons and varicose terminals in the epicardial and myocardial layers and around blood vessels. TH-IR axons and varicose terminals were observed to densely innervate the SA node and the junctions of the vena cava and pulmonary veins with the atria. In ICG on the dorsal surface of the atria, a subpopulation of PNs was strongly TH-IR. In addition, strongly TH-IR SIF cells were observed within ICG or adjacent to TH-IR axon bundles. In contrast to TH-IR axons in the stomach and small intestine where TH-IR axons formed extensive varicose terminals in myenteric ganglia. TH-IR axons in the atria were not observed to form varicose terminals encircling PNs. TH-IR nerve bundles and axons branching from the bundles ran through ICG. There is a possibility that TH-IR neurons in the ICG would project processes, but more studies are needed to delineate their functions and determine whether or not they innervate any targets. In the ventricles and IVS, TH-IR axons and varicose terminals were also found in the epicardial and myocardial layers and around blood vessels. Large TH-IR bundles entered the ventricles and IVS, branched out and innervated the whole ventricles and IVS from the base to the apex.

4.1 Our methodology vs. tissue clearing

Our method of thick tissue flat-mount processing and imaging has several advantages over traditional histological sectioning techniques, and *de facto* allowed us to examine the distribution and morphology of TH-IR axon innervation while preserving the integrity of the whole atrial flat-mount and large ventricular preparations. Prior studies used sectioned heart preparations or small partial flat-mounts of regions of the heart, which disrupted the continuity of axons and terminals (Ajijola et al., 2015; Freeman et al., 2014; Hanna et al., 2021; Hoover et al., 2009; Inokaitis et al., 2016; Richardson et al., 2003). More recently, tissue-clearing allowed the advancement of three-dimensional (3D) visualization of the heart innervation and provided tissues with high transparency which facilitated the knowledge of the 3D structures (Rajendran et al., 2019; Yokoyama et al., 2017). It should be recognized that this novel technique enabled deep imaging of large tissues and improved the penetration of laser light, which gives insights into the structures more precisely. There are many available tissue-clearing methods that can be used for various purposes. Each of these methods has advantages and disadvantages that were thoroughly reviewed by (Kolesová et al., 2021). Among the most common families of tissue clearing are Disco, CUBIC, and Clarity. They differ in cost, complexity, speed, conservation of protein-based fluorescence, and compatibility with immunostaining. Although tissue clearing enables the visualization of entire organs in whole-mount preparation while avoiding any distortion of the tissue, there is no one universal method for all applications. Two particular studies (Yokoyama et al., 2017, Rajendran et al., 2019) showed novel tissue-clearing techniques to visualize the innervation of intact hearts in 3D, but the details of innervation (especially in the atria) and the multiple cardiac targets that we were able to identify in our work could not be identified in either study. It is essential to identify the targets which are influenced by nerves, so the removal of background staining of target cells in tissue-clearing hinders the visualization of the nerve/effector interface. Another limitation of tissue clearing lies in its limited feasibility to visualize other cardiac targets such as ganglion cells, muscles, and adipocytes as well as the fine details of axons and terminals.

Also, tissue clearing requires extremely difficult protocols, long time, expensive imaging equipment, and the need to try several methods to achieve the best results. Our method is simple, relatively fast, inexpensive, and can be performed with conventional microscopy equipment. Our current methodology overcomes these limitations and allows for large-scale morphological characterization of these structures with high resolution. The high resolution we used allowed the visualization of the rich TH-IR axon innervation and enabled us to identify more fine details than available methods had allowed us to. One limitation of our study which must be acknowledged is the impact of flattening the tissue on the 3D structure. The novelty of this study lies in the creation of a comprehensive map where the continuity of the nerves can be preserved and the progression of the axons from being non-varicose in large bundles to being varicose at the targeted location such as the blood vessels, muscles, and fat. It set a solid foundation for future functional studies. We believe that a combination of our flat-mount approach along with tissue clearing can be very robust in avoiding the limitation of each method and potentially enrich our knowledge tremendously of the heart innervation and the different cardiac targets.

4.2 Origin of TH-IR axons in the heart: Extrinsic and Intrinsic

It has been well documented that the majority of the sympathetic postganglionic neurons [e.g. stellate ganglia (SG), middle and superior ganglia] are TH-IR (Pardini et al., 1989; Rajendran et al., 2019). In our study, we labeled the SG for TH, and found that most of the SG neurons were TH-IR (not shown), further supporting the assumption that cardiac TH-IR axons originate from the SG. Although the primary source of TH-IR axons in the heart is extrinsic in nature, there is an ICG component that merits further investigation. In each animal, we observed a subpopulation of ICG PNs that were TH-IR. Similar findings were previously reported in the ICG of mice (Hoard et al., 2008). TH is also expressed at low levels in the sensory neurons of the dorsal root ganglia (DRG) and nodose ganglia (NG) in a variety of animals (Sapio et al., 2020). The presence of TH-IR neurons in these extrinsic and intrinsic ganglia necessitates further investigation since their function remains poorly understood.

Although a subpopulation of ICG PNs contains TH, such neurons may be unable to functionally release catecholaminergic neurotransmitters due to the lack of vesicular monoamine transporter 2 (VMAT2) expression, a protein that is required for the transport of dopamine (DA) into synaptic vesicles where the DA is converted to norepinephrine (NE) by dopamine beta hydroxylase (Bamford et al., 2004; Hoover et al., 2009; Sulzer et al., 2005). Although studies of mouse ICG showed no expression of VMAT2 (Hoard et al., 2008), colocalization of TH and VMAT2 emerged in a few human ICG (Hoover et al., 2009), indicating species differences. Further functional studies are needed to elucidate the function of TH-IR ICG neurons in mice. In addition, the expression of TH positive neurons in DRG and NG was transient or nonfunctional because they lack the enzymes for catecholamine metabolism, storage and release (Brumovsky, 2016; Kummer et al.,1990). In contrast, these enzymes are expressed in the TH-IR neurons of mouse SG, indicating their functional capability (Kokubun et al., 2019; Kummer et al., 1990).

4.3 TH-IR axons: distribution and morphology in the atrial and the ventricular preparations at the single cell/axon scale

We observed dense TH-IR innervation throughout the atria, including nodal and contractile regions, the auricles and the junction of the large veins with the myocardium. These findings suggest that catecholaminergic axons (likely from the sympathetic nervous system) exert a large degree of control over cardiac functions. The distribution of TH-IR axons in the atria suggests that sympathetic efferent axons may exert differential control over different cardiac targets. Additionally, our methods overcame the thickness limitation in the ventricles and allowed us to visualize the intricate structures of TH-IR innervation in both ventricles and IVS. Partial flat-mounts of the ventricles and IVS showed unprecedented resolution of TH-IR axon innervation. All of the present improvements will pave the way for determining the sympathetic efferent innervation of the flat-mount of whole ventricles by optimizing these methods to incorporate whole left and right ventricles and IVS. Furthermore, our data provide an anatomical foundation for quantitative assessment of normal and disease-induced remodeling of TH-IR innervation in different regions of the heart.

4.4 TH-IR innervation of vasculature and adipose tissue

Sympathetic control is key to maintaining vascular tone, blood pressure, and cardiovascular homeostasis and overactivity of sympathetic nerves leads to vascular dysfunction (Sheng and Zhu, 2018). TH-IR axons innervating the vasculature were observed near the atria and ventricles, and the great vessels (IVC, SVC, LPCV, and PVs) were densely innervated by the TH-IR axon network. Within the atria and ventricles, TH-IR axons ran closely along small blood vessels. Notably, the current study showed an unprecedentedly high density of TH-IR axon innervation of blood vessels. However, we did not verify whether these small blood vessels were small arterioles/arteries or venules/veins. Therefore, further research should be undertaken to investigate the specific type of blood vessels and the functional implications of TH-IR axon innervation of different blood vessels.

TH-IR axonal varicosities ran along the circumference of individual adipocytes and in between them indicating the direct association of TH-IR axons and adipocytes. There are mainly two types of fat: white adipose tissue (WAT) which serves a role in the storage of triglycerides and metabolizing lipids, and brown adipose tissue (BAT) which underlies production of heat to maintain body temperature, respectively (Symonds et al., 2018). The sympathetic nerves are essential for optimal WAT and BAT functions (Bartness et al., 2014; Morrison et al., 2014). The presence of WAT and BAT has been found in the epicardial and thoracic regions (Bartness et al., 2014; Iacobellis, 2021; Morrison et al., 2014; Padilla et al., 2013; Sacks et al., 2013). Recently, it was noted that epicardial fat is primarily WAT but displays BAT features as well (Iacobellis, 2021). More studies are needed to classify the type of adipocytes near the heart and the role of sympathetic innervation in those regions.

4.5 TH-IR axons in the ICG vs. myenteric plexus

TH-IR bundles and axons mainly passed through ICG rather than forming synaptic connections with individual ICG PNs, whereas only some axons might have few varicose connections with PNs, if any. This observation contrasts with previous findings in the ICN of guinea pigs and rats where some TH-IR axons formed terminal varicosities around the PNs (Parsons, 2004; Richardson et al., 2003). However, our findings are consistent with a recent study (Hanna et al., 2021) that showed TH-IR nerve fibers pass through the porcine cardiac ganglia without forming varicosities surrounding the neurons. Our recent observation in C57BL/6J mice showed a similar result (not shown). We assume that the scarcity of major TH-IR synaptic-like varicosities around ICG PNs indicates that extrinsic sympathetic postganglionic neurons provide great control over the other cardiac tissues (muscles, blood vessels, and adipocytes). In the gastrointestinal tract, however, the myenteric neurons are commonly and densely innervated by TH-IR axons, which is demonstrated by numerous short, varicose, synaptic-like terminal structures around the myenteric neurons. This observation is consistent with Powley and his colleagues who reported that celiac postganglionic sympathetic axons formed numerous varicose endings around individual myenteric neurons in the stomach after tracer injection into the celiac ganglia in rats (Walter et al., 2016). Thus, it appears that sympathetic efferent innervation of the heart and stomach have different patterns. The scarcity of TH-IR synaptic-like varicosities around PNs suggests that they are not innervated by other TH-IR PNs, at least in FVB mice. Whether sympathetic efferent axons significantly innervate ICG PNs in other species should therefore be explored. Of note, most ICG were observed at the LA-PV junction which has been shown to be critical for the induction of atrial fibrillation (Lim et al., 2011; Lim et al., 2011b).

As in previous experiments in rats (Cheng et al., 1997b; Cheng et al., 1999), we also found that many SIF cells (identified by their intense TH-IR and diameter < 10 μm) are present in the heart. They are primarily found in small clusters associated with ICG PNs or in large clusters near bundles of TH-IR axons. The function of SIF cells and their innervation pattern is not well understood, and their function is still debatable (Cheng et al., 1997a; Huber, 2006). SIF cells are found in large numbers in the carotid bodies of mice, where their role is believed to be chemosensory in nature (Doupe et al., 1985; Kvetnansky et al., 2009). It has been suggested that SIF cells in the heart may have chemosensory functions or serve information to ICG PNs (Matthews, 1989; Takaki et al., 2015). Functional studies are needed to determine the role of SIF cells in the heart.

4.6 Functional implications

Our work demonstrated the large-scale morphological and distribution characteristics of catecholaminergic innervation in the atria and ventricles and established a flat-mount approach to investigate detailed cardiac neuroanatomy in future studies. Using our approach would be valuable for future quantitative studies to further investigate the regional differences of TH-IR axon innervation in the heart and the interaction with different cardiac targets. Additionally, considering the role of TH as a key enzyme in the synthesis of catecholamines, its alteration is associated with pathological conditions including CVDs (hypertension, heart failure, myocardial infarction, atrial fibrillation) (Li et al., 2013; Nisimura et al., 2020), and sleep breathing disorders like sleep apnea (Bathina et al., 2013). Therefore, basic knowledge of the normal anatomical structure of cardiac TH-IR axon innervation is a crucial step for establishing a baseline to use when evaluating potential remodeling induced by different pathological conditions. We have previously demonstrated the remodeling of vagal efferent and afferent axons in diseases including aging, diabetes, and chronic intermittent hypoxia (a hallmark of sleep apnea) (Ai et al., 2009, Ai et al., 2007, Cheng, 2017). In future studies, we will extend these works by employing the methods described here to better evaluate cardiac autonomic remodeling in these conditions. Furthermore, our approach could be used to understand the anatomical heterogeneity in normal and diseased conditions, which may eventually contribute to the improvement of the selectivity of neuromodulation therapy. Collectively, our data lays the groundwork for future functional studies that will correlate the structural and physiological features of cardiac catecholaminergic innervation and can be used concomitantly with clarity methods to create a complete sympathetic cardiac-brain atlas.

4.7 Limitations

Although the whole-mount immunolabeling technique described here has many advantages over traditional methods using tissue sections, some limitations are worth noting. The primary focus of this study was to develop a method to immunolabel neural structures while preserving the network-level anatomical, but studies employing this method will benefit from designing unique strategies of quantification customized to their hypothesis and structures being labeled. Also, the percentage of TH-IR neurons subpopulation of ICG assessments will be needed and may be improved by using a pan-neuronal marker to label TH-positive neurons (Leger et al., 1999, Hanna et al., 2017). Flattening of the whole mount could impact the tissue’s 3D structural integrity. Therefore, tracing the nerves and integrating the reconstructed nerves into a 3D heart scaffold could be a potential solution to restore the 3D integrity of the axonal structures. Combining our approach with tissue-clearing techniques could also be a robust method to provide a comprehensive map of cardiac innervation. Another limitation would be the uncertainty in determining the source of TH-IR fibers. Future experiments that use anterograde tracing injected into the stellate ganglia along with TH staining could potentially fill this gap to specifically label axons originating from the sympathetic ganglia.

5. Summary

This study implemented a novel approach that enabled the assessment of the distribution and morphology of TH-IR axons in the flat-mount of the whole mouse atria and large ventricular/IVS preparations at a single cell/axon/varicosity scale. Our main findings are summarized in (Fig. 16). In the atria, multiple large extrinsic bundles of TH-IR axons entered the atria, traveled through the ICG, and bifurcated multiple times, eventually innervating the epicardial layer with complex TH-IR axon networks that extended into the myocardial layer. In addition, many TH-IR axons innervated vasculature and adipose cells. The atria contained multiple ICG, and most ICG were located on the dorsal surface of the left atrium. Within the ICG, some neurons expressed immunoreactivity to TH and TH-IR axons mainly ran through the ICG without forming direct contacts. Furthermore, many SIF cell clusters were found in or near ICG and were also immunoreactive to TH. However, the functions of TH-IR neurons and SIF cells in the ICG are not clear and should be further investigated. Notwithstanding, the extensive, diverse and complex distribution of TH-containing nerve endings in or around the SA and AV nodes, muscles, and blood vessels supports the concept that catecholaminergic or sympathetic axons play an important role in the neural regulation of SA node activity, AV conduction, heart rate, cardiac muscle contractility, and blood flow. In the ventricles and IVS, TH-IR bundles entered the ventricles and IVS, branched out, and ramified into individual axons. These axons formed dense innervation of the entire ventricles and IVS extending from the base towards the apex. In the future, it will be important to conduct quantitative analysis to elucidate the topographical organization and structures of sympathetic efferent neurons innervating the whole heart (atria, ventricles, and IVS) using a combination of catecholaminergic labeling and anterograde tracer injection into the sympathetic ganglia, which will eventually lead to a more complete mapping of the sympathetic efferent innervation of the whole heart. This study will set the foundation for functional mapping and quantitative assessment of topographical TH-IR axon innervation of the whole heart.

Acknowledgments

This work was supported by NIH 1 U01 NS113867-01 and NIH R15 1R15HL137143-01A1 (ZJC). We thank Dr. Phillips RJ for his expertise and assistance to optimize our methodology. We also thank Dr. John Tompkins for his insights and we thank the following individuals for their help in editing the manuscript: Kohlton Bendowski, Duyen Nguyen and Anas Mistareehi.

Data availability

The datasets used and analyzed during the current study available from the corresponding author on reasonable request.

References

Ai J, Epstein PN, Gozal D, Yang B, Wurster R. and Cheng ZJ (2007a). Morphology and topography of nucleus ambiguus projections to cardiac ganglia in rats and mice. Neuroscience, 149, 845–860. [PubMed: 17942236]

Ai J, Gozal D, Li L, Wead WB, Chapleau MW, Wurster R, Yang B, Li H, Liu R. and Cheng Z. (2007b). Degeneration of vagal efferent axons and terminals in cardiac ganglia of aged rats. Journal of Comparative Neurology, 504, 74–88. [PubMed: 17614301]

Ai J, Wurster RD, Harden SW and Cheng ZJ (2009). Vagal afferent innervation and remodeling in the aortic arch of young-adult fischer 344 rats following chronic intermittent hypoxia. Neuroscience, 164, 658–666. [PubMed: 19580847]

Ajijola OA, Yagishita D, Reddy NK, Yamakawa K, Vaseghi M, Downs AM, Hoover DB, Ardell JL and Shivkumar K. (2015). Remodeling of stellate ganglion neurons after spatially targeted myocardial infarction: Neuropeptide and morphologic changes. Heart Rhythm, 12, 1027–1035. [PubMed: 25640636]

Ardell JL, Andresen MC, Armour JA, Billman GE, Chen PS, Foreman RD, Herring N, O'Leary DS, Sabbah HN, Schultz HD, Sunagawa K. and Zucker IH (2016). Translational neurocardiology: preclinical models and cardioneural integrative aspects. J Physiol, 594, 3877–3909. [PubMed: 27098459]

Armour JA (1999). Myocardial ischaemia and the cardiac nervous system. Cardiovascular Research, 41, 41–54. [PubMed: 10325952]

Armour JA (2008). Potential clinical relevance of the 'little brain' on the mammalian heart. Exp Physiol, 93, 165–176. [PubMed: 17981929]

Bartness TJ, Liu Y, Shrestha YB and Ryu V. (2014). Neural innervation of white adipose tissue and the control of lipolysis. Front Neuroendocrinol, 35, 473–493. [PubMed: 24736043]

Bathina CS, Rajulapati A, Franzke M, Yamamoto K, Cunningham JT and Mifflin S. (2013). Knockdown of tyrosine hydroxylase in the nucleus of the solitary tract reduces elevated blood pressure during chronic intermittent hypoxia. Am J Physiol Regul Integr Comp Physiol, 305, R1031–1039. [PubMed: 24049117]

Birand A. (2008). [Intrinsic cardiac ganglia]. Anadolu Kardiyol Derg, 8, 451–454. [PubMed: 19103543]

Brown TC, Bond CE and Hoover DB (2018). Variable expression of GFP in different populations of peripheral cholinergic neurons of ChATBAC-eGFP transgenic mice. Autonomic Neuroscience, 210, 44–54. [PubMed: 29288022]

Brumovsky PR (2016). Dorsal root ganglion neurons and tyrosine hydroxylase--an intriguing association with implications for sensation and pain. Pain, 157, 314–320. [PubMed: 26447702]

Calupca MA, Locknar SA, Zhang L, Harrison TA, Hoover DB and Parsons RL (2001). Distribution of cocaine- and amphetamine-regulated transcript peptide in the guinea pig intrinsic cardiac nervous system and colocalization with neuropeptides or transmitter synthetic enzymes. J Comp Neurol, 439, 73–86. [PubMed: 11579383]

Chen J, Gu H, Wurster RD and Cheng ZJ (2021). The protective role of SOD1 overexpression in central mediation of bradycardia following chronic intermittent hypoxia in mice. Am J Physiol Regul Integr Comp Physiol, 320, R317–r330. [PubMed: 33296277]

Cheng Z. (2017). Vagal cardiac efferent innervation in F344 rats: Effects of chronic intermittent hypoxia. Autonomic Neuroscience, 203, 9–16. [PubMed: 27839717]

Cheng Z. and Powley TL (2000). Nucleus ambiguus projections to cardiac ganglia of rat atria: An anterograde tracing study. Journal of Comparative Neurology, 424, 588–606. [PubMed: 10931483]

Cheng Z, Powley TL, Schwaber JS and Doyle FJ 3rd. (1997a). A laser confocal microscopic study of vagal afferent innervation of rat aortic arch: chemoreceptors as well as baroreceptors. J Auton Nerv Syst, 67, 1–14. [PubMed: 9470139]

Cheng Z, Powley TL, Schwaber JS and Doyle FJ 3rd. (1997b). Vagal afferent innervation of the atria of the rat heart reconstructed with confocal microscopy. J Comp Neurol, 381, 1–17. [PubMed: 9087415]

Cheng Z, Powley TL, Schwaber JS and Doyle FJ 3rd. (1999). Projections of the dorsal motor nucleus of the vagus to cardiac ganglia of rat atria: an anterograde tracing study. J Comp Neurol, 410, 320–341. [PubMed: 10414536]

Cheng Z, Zhang H, Guo SZ, Wurster R. and Gozal D. (2004). Differential control over postganglionic neurons in rat cardiac ganglia by NA and DmnX neurons: anatomical evidence. American Journal of Physiology-Regulatory, Integrative and Comparative Physiology, 286, R625–R633. [PubMed: 14644755]

Doupe AJ, Patterson PH and Landis SC (1985). Small intensely fluorescent cells in culture: role of glucocorticoids and growth factors in their development and interconversions with other neural crest derivatives. J Neurosci, 5, 2143–2160. [PubMed: 4020433]

Fedele L. and Brand T. (2020). The Intrinsic Cardiac Nervous System and Its Role in Cardiac Pacemaking and Conduction. J Cardiovasc Dev Dis, 7.

Freeman K, Tao W, Sun H, Soonpaa MH and Rubart M. (2014). In situ three-dimensional reconstruction of mouse heart sympathetic innervation by two-photon excitation fluorescence imaging. J Neurosci Methods, 221, 48–61. [PubMed: 24056230]

Gu H, Epstein PN, Li L, Wurster RD and Cheng ZJ (2008). Functional changes in baroreceptor afferent, central and efferent components of the baroreflex circuitry in type 1 diabetic mice (OVE26). Neuroscience, 152, 741–752. [PubMed: 18328631]

Gu H, Lin M, Liu J, Gozal D, Scrogin KE, Wurster R, Chapleau MW, Ma X. and Cheng Z. (2007). Selective impairment of central mediation of baroreflex in anesthetized young adult Fischer 344 rats after chronic intermittent hypoxia. American Journal of Physiology-Heart and Circulatory Physiology, 293, H2809–H2818. [PubMed: 17693540]

Hanna P, Dacey MJ, Brennan J, Moss A, Robbins S, Achanta S, Biscola NP, Swid MA, Rajendran PS, Mori S, Hadaya JE, Smith EH, Peirce SG, Chen J, Havton LA, Cheng ZJ, Vadigepalli R, Schwaber J, Lux RL, Efimov I, Tompkins JD, Hoover DB, Ardell JL and Shivkumar K. (2021). Innervation and Neuronal Control of the Mammalian Sinoatrial Node a Comprehensive Atlas. Circ Res, 128, 1279–1296. [PubMed: 33629877]

Hanna P, Rajendran PS, Ajijola OA, Vaseghi M, Andrew Armour J, Ardell JL and Shivkumar K. (2017). Cardiac neuroanatomy - Imaging nerves to define functional control. Auton Neurosci, 207, 48–58. [PubMed: 28802636]

Herring N. and Paterson DJ (2021). The Heart's Little Brain. Circulation Research, 128, 12971299.

Hibberd TJ, Yew WP, Chen BN, Costa M, Brookes SJ and Spencer NJ (2020). A Novel Mode of Sympathetic Reflex Activation Mediated by the Enteric Nervous System. eNeuro, 7.

Hoard JL, Hoover DB, Mabe AM, Blakely RD, Feng N. and Paolocci N. (2008). Cholinergic neurons of mouse intrinsic cardiac ganglia contain noradrenergic enzymes, norepinephrine transporters, and the neurotrophin receptors tropomyosin-related kinase A and p75. Neuroscience, 156, 129–142. [PubMed: 18674600]

Hoover DB, Isaacs ER, Jacques F, Hoard JL, Pagé P. and Armour JA (2009). Localization of multiple neurotransmitters in surgically derived specimens of human atrial ganglia. Neuroscience, 164, 1170–1179. [PubMed: 19747529]

Huber K. (2006). The sympathoadrenal cell lineage: specification, diversification, and new perspectives. Dev Biol, 298, 335–343. [PubMed: 16928368]

Iacobellis G. (2021). Aging Effects on Epicardial Adipose Tissue. Frontiers in Aging, 2.

Inokaitis H, Pauziene N, Rysevaite-Kyguoliene K. and Pauza DH (2016). Innervation of sinoatrial nodal cells in the rabbit. Ann Anat, 205, 113–121. [PubMed: 27045595]

Kokubun S, Sato T, Yajima T. and Ichikawa H. (2019). Distribution of postganglionic neurons which contain dopamine β-hydroxylase, tyrosine hydroxylase, neuropeptide Y and vasoactive intestinal polypeptide in the human middle cervical ganglion. Tissue Cell, 58, 42–50. [PubMed: 31133245]

Kolesová H, Olejníčková V, Kvasilová A, Gregorovičová M. and Sedmera D. (2021). Tissue clearing and imaging methods for cardiovascular development. iScience, 24, 102387.

Kummer W, Gibbins IL, Stefan P. and Kapoor V. (1990). Catecholamines and catecholaminesynthesizing enzymes in guinea-pig sensory ganglia. Cell Tissue Res, 261, 595–606. [PubMed: 1978803]

Kvetnansky R, Sabban EL and Palkovits M. (2009). Catecholaminergic Systems in Stress: Structural and Molecular Genetic Approaches. Physiological Reviews, 89, 535–606. [PubMed: 19342614]

Leger J, Croll RP and Smith FM (1999). Regional distribution and extrinsic innervation of intrinsic cardiac neurons in the guinea pig. J Comp Neurol, 407, 303–317. [PubMed: 10320213]

Li L, Hatcher JT, Hoover DB, Gu H, Wurster RD and Cheng ZJ (2014). Distribution and morphology of calcitonin gene-related peptide and substance P immunoreactive axons in the whole-mount atria of mice. Auton Neurosci, 181, 37–48. [PubMed: 24433968]

Li L, Huang C, Ai J, Yan B, Gu H, Ma Z, Li AY, Xinyan S, Harden SW, Hatcher JT, Wurster RD and Cheng ZJ (2010). Structural remodeling of vagal afferent innervation of aortic arch and nucleus ambiguus (NA) projections to cardiac ganglia in a transgenic mouse model of type 1 diabetes (OVE26). J Comp Neurol, 518, 2771–2793. [PubMed: 20506475]

Lim PB, Malcolme-Lawes LC, Stuber T, Kojodjojo P, Wright IJ, Francis DP, Wyn Davies D, Peters NS and Kanagaratnam P. (2011a). Stimulation of the intrinsic cardiac autonomic nervous system results in a gradient of fibrillatory cycle length shortening across the atria during atrial fibrillation in humans. J Cardiovasc Electrophysiol, 22, 1224–1231. [PubMed: 21615814]

Lim PB, Malcolme-Lawes LC, Stuber T, Wright I, Francis DP, Davies DW, Peters NS and Kanagaratnam P. (2011b). Intrinsic cardiac autonomic stimulation induces pulmonary vein ectopy and triggers atrial fibrillation in humans. J Cardiovasc Electrophysiol, 22, 638–646. [PubMed: 21235671]

Lin M, Ai J, Li L, Huang C, Chapleau MW, Liu R, Gozal D, Wead WB, Wurster RD and Cheng Z. (2008). Structural remodeling of nucleus ambiguus projections to cardiac ganglia following chronic intermittent hypoxia in C57BL/6J mice. J Comp Neurol, 509, 103–117. [PubMed: 18425809]

Matthews MR (1989). Small, intensely fluorescent cells and the paraneuron concept. J Electron Microsc Tech, 12, 408–416. [PubMed: 2671307]

Morrison SF, Madden CJ and Tupone D. (2014). Central neural regulation of brown adipose tissue thermogenesis and energy expenditure. Cell Metab, 19, 741–756. [PubMed: 24630813]

Nisimura LM, Bousquet P, Muccillo F, Tibirica E. and Garzoni LR (2020). Tyrosine hydroxylase and β2-adrenergic receptor expression in leukocytes of spontaneously hypertensive rats: putative peripheral markers of central sympathetic activity. Braz J Med Biol Res, 53, e9615. [PubMed: 33146287]

Padilla J, Jenkins NT, Vieira-Potter VJ and Laughlin MH (2013). Divergent phenotype of rat thoracic and abdominal perivascular adipose tissues. Am J Physiol Regul Integr Comp Physiol, 304, R543–552. [PubMed: 23389108]

Pardini BJ, Lund DD and Schmid PG (1989). Organization of the sympathetic postganglionic innervation of the rat heart. J Auton Nerv Syst, 28, 193–201. [PubMed: 2628461]

Parker DR, Wiklendt L, Humenick A, Chen BN, Sia TC, Wattchow DA, Dinning PG and Brookes SJH (2022). Sympathetic Pathways Target Cholinergic Neurons in the Human Colonic Myenteric Plexus. Frontiers in Neuroscience, 16.

Pauza DH, Rysevaite K, Inokaitis H, Jokubauskas M, Pauza AG, Brack KE and Pauziene N. (2014). Innervation of sinoatrial nodal cardiomyocytes in mouse. A combined approach using immunofluorescent and electron microscopy. J Mol Cell Cardiol, 75, 188–197. [PubMed: 25101952]

Pauza DH, Saburkina I, Rysevaite K, Inokaitis H, Jokubauskas M, Jalife J. and Pauziene N. (2013). Neuroanatomy of the murine cardiac conduction system: a combined stereomicroscopic and fluorescence immunohistochemical study. Auton Neurosci, 176, 32–47. [PubMed: 23403121]

Powley TL, Hudson CN, McAdams JL, Baronowsky EA and Phillips RJ (2016). Vagal Intramuscular Arrays: The Specialized Mechanoreceptor Arbors That Innervate the Smooth Muscle Layers of the Stomach Examined in the Rat. Journal of Comparative Neurology, 524, 713–737. [PubMed: 26355387]

Rajendran PS, Challis RC, Fowlkes CC, Hanna P, Tompkins JD, Jordan MC, Hiyari S, Gabris-Weber BA, Greenbaum A, Chan KY, Deverman BE, Münzberg H, Ardell JL, Salama G, Gradinaru V. and Shivkumar K. (2019). Identification of peripheral neural circuits that regulate heart rate using optogenetic and viral vector strategies. Nature Communications, 10, 1944.

Richardson RJ, Grkovic I. and Anderson CR (2003). Immunohistochemical analysis of intracardiac ganglia of the rat heart. Cell Tissue Res, 314, 337–350. [PubMed: 14523644]

Rysevaite K, Saburkina I, Pauziene N, Noujaim SF, Jalife J. and Pauza DH (2011). Morphologic pattern of the intrinsic ganglionated nerve plexus in mouse heart. Heart Rhythm, 8, 448–454. [PubMed: 21075216]

Sacks HS, Fain JN, Bahouth SW, Ojha S, Frontini A, Budge H, Cinti S. and Symonds ME (2013). Adult epicardial fat exhibits beige features. J Clin Endocrinol Metab, 98, E1448–1455. [PubMed: 23824424]

Sapio MR, Vazquez FA, Loydpierson AJ, Maric D, Kim JJ, LaPaglia DM, Puhl HL, Lu VB, Ikeda SR, Mannes AJ and Iadarola MJ (2020). Comparative Analysis of Dorsal Root, Nodose and Sympathetic Ganglia for the Development of New Analgesics. Front Neurosci, 14, 615362. [PubMed: 33424545]

Sheng Y. and Zhu L. (2018). The crosstalk between autonomic nervous system and blood vessels. Int J Physiol Pathophysiol Pharmacol, 10, 17–28. [PubMed: 29593847]

Shivkumar K, Ajijola OA, Anand I, Armour JA, Chen PS, Esler M, De Ferrari GM, Fishbein MC, Goldberger JJ, Harper RM, Joyner MJ, Khalsa SS, Kumar R, Lane R, Mahajan A, Po S, Schwartz PJ, Somers VK, Valderrabano M, Vaseghi M. and Zipes DP (2016). Clinical neurocardiology defining the value of neuroscience-based cardiovascular therapeutics. J Physiol, 594, 3911–3954. [PubMed: 27114333]

Symonds ME, Aldiss P, Pope M. and Budge H. (2018). Recent advances in our understanding of brown and beige adipose tissue: the good fat that keeps you healthy. F1000Res, 7.

Takaki F, Nakamuta N, Kusakabe T. and Yamamoto Y. (2015). Sympathetic and sensory innervation of small intensely fluorescent (SIF) cells in rat superior cervical ganglion. Cell Tissue Res, 359, 441–451. [PubMed: 25416508]

Walter GC, Phillips RJ, McAdams JL and Powley TL (2016). Individual sympathetic postganglionic neurons coinnervate myenteric ganglia and smooth muscle layers in the gastrointestinal tract of the rat. J Comp Neurol, 524, 2577–2603. [PubMed: 26850701]

Yan B, Li L, Harden SW, Gozal D, Lin Y, Wead WB, Wurster RD and Cheng Z. (2009). Chronic intermittent hypoxia impairs heart rate responses to AMPA and NMDA and induces loss of glutamate receptor neurons in nucleus ambiguus of F344 rats. American Journal of Physiology-Regulatory, Integrative and Comparative Physiology, 296, R299–R308. [PubMed: 19020286]

Yan B, Soukhova-O’Hare GK, Li L, Lin Y, Gozal D, Wead WB, Wurster RD and Cheng ZJ (2008). Attenuation of heart rate control and neural degeneration in nucleus ambiguus following chronic intermittent hypoxia in young adult Fischer 344 rats. Neuroscience, 153, 709–720. [PubMed: 18417294]

Yokoyama T, Lee J-K, Miwa K, Opthof T, Tomoyama S, Nakanishi H, Yoshida A, Yasui H, Iida T, Miyagawa S, Okabe S, Sawa Y, Sakata Y. and Komuro I. (2017). Quantification of sympathetic hyperinnervation and denervation after myocardial infarction by three-dimensional assessment of the cardiac sympathetic network in cleared transparent murine hearts. PLOS ONE, 12, e0182072.

Zandstra TE, Notenboom RGE, Wink J, Kiès P, Vliegen HW, Egorova AD, Schalij MJ, De Ruiter MC and Jongbloed MRM (2021). Asymmetry and Heterogeneity: Part and Parcel in Cardiac Autonomic Innervation and Function. Frontiers in Physiology, 12.

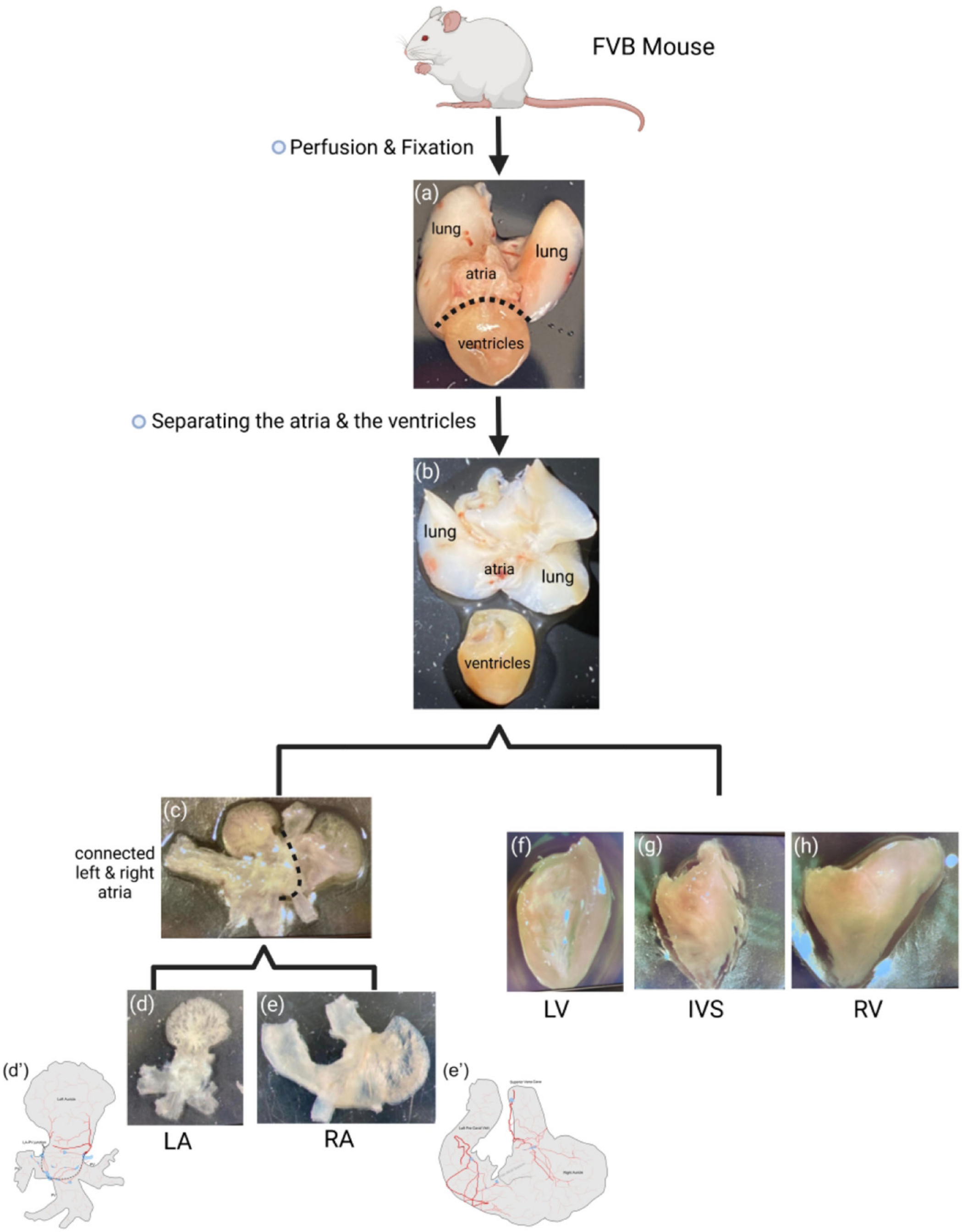

Figure 1.

Preparation of flat-mounts of a mouse heart for TH immunohistochemistry. **(a)**. A heart with attached lungs, trachea, and esophagus was collected after perfusion. **(b)**. The heart was separated from other structures and followed by separation of the atria and ventricles. **(c).** The brown adipose tissue and aortic arch were removed to expose the connected RA and LA. **(d,e).** The LA (**d**) with pulmonary veins were separated from the RA (**e**) with SVC, LPCV, and IVC. The primary features we observed after staining were shown in a schematic of RA and LA **(d',e')**. The LV (**f**) and RV (**h**) were separated by cutting along the interventricular septum (IVS, **g**). *RA: right atrium, LA: left atrium, RV: right ventricle, LV: left ventricle, IVS: interventricular septum*.

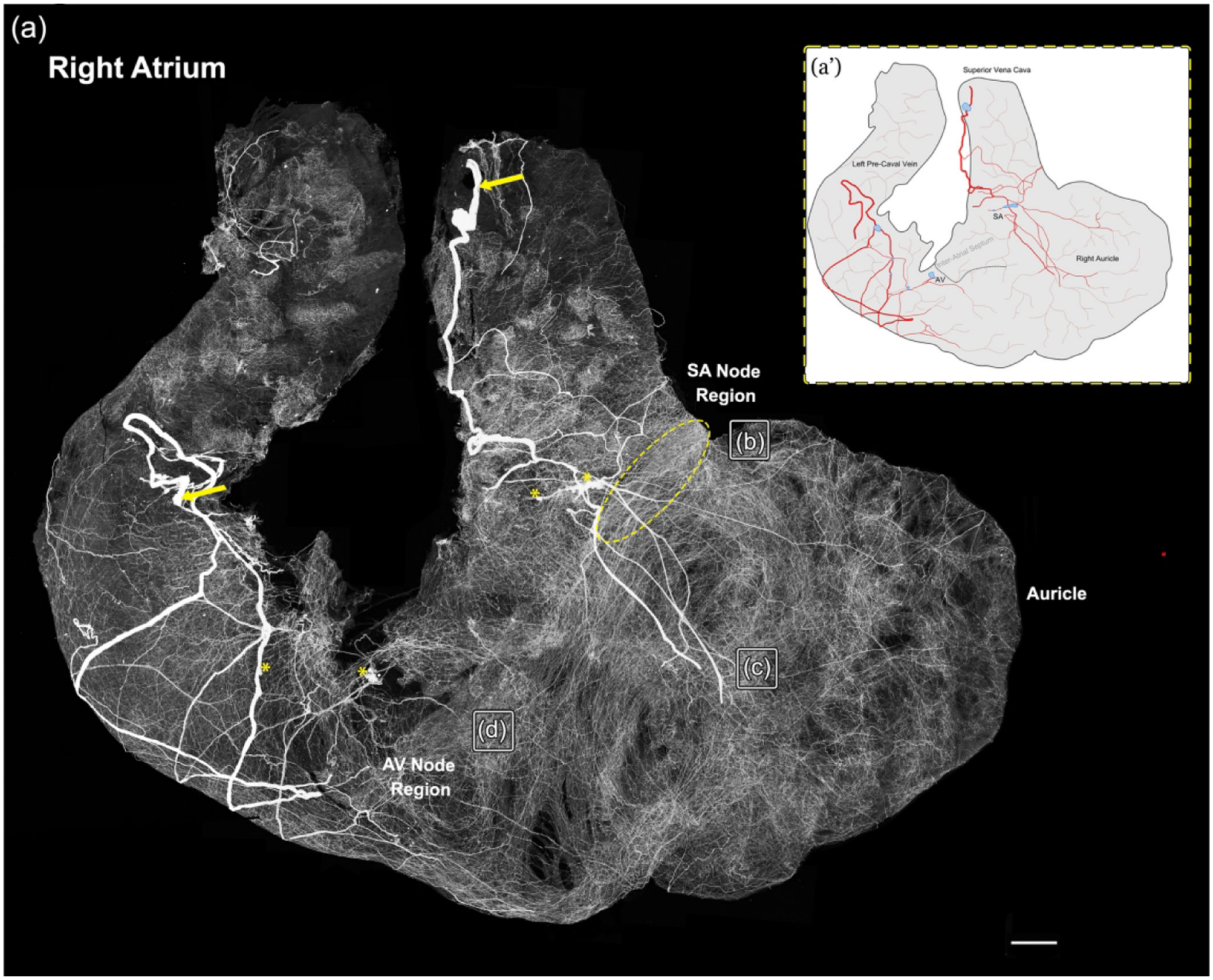

Figure 2.

TH-IR innervation of the whole right atrium flat-mount

(a) A montage made of a few hundred all-in-focus maximum confocal projection images demonstrating the catecholaminergic (TH-IR) axon (white fibers) innervation of the whole RA at single cell/axon/varicosity resolution. Large TH-IR bundles (yellow arrows) entered the RA through the SVC and LPCV. ICG (yellow asterisks) situated near the base of the SVC alongside the TH-IR bundle or the point of attachment to the LA. (a') Schematic diagram to designate primary features. Large bundles of TH-IR axons (thick red lines) which bifurcated into smaller bundles (thin red lines) and ultimately innervated the atria with long, varicose, single axon terminals. Ganglia (blue regions), some of which were cut in the process of separating the LA and RA. Boxed regions **(b**, **c**, and **d)** were enlarged and displayed in (Figure 4 b, c, and d, respectively). *TH-IR: Tyrosine hydroxylase immunoreactive; RA: right atrium, LA: left atrium, ICG: intrinsic cardiac ganglia, SVC: superior vena cava, LPCV: left pre-caval vein; SA: sinoatrial (in the schematic it indicates* the ganglion close to the sino-atrial node region*; AV: atrioventricular (in the schematic in indicates* the ganglion close to the atrio-ventricular node region) Scale bar: 500µm.

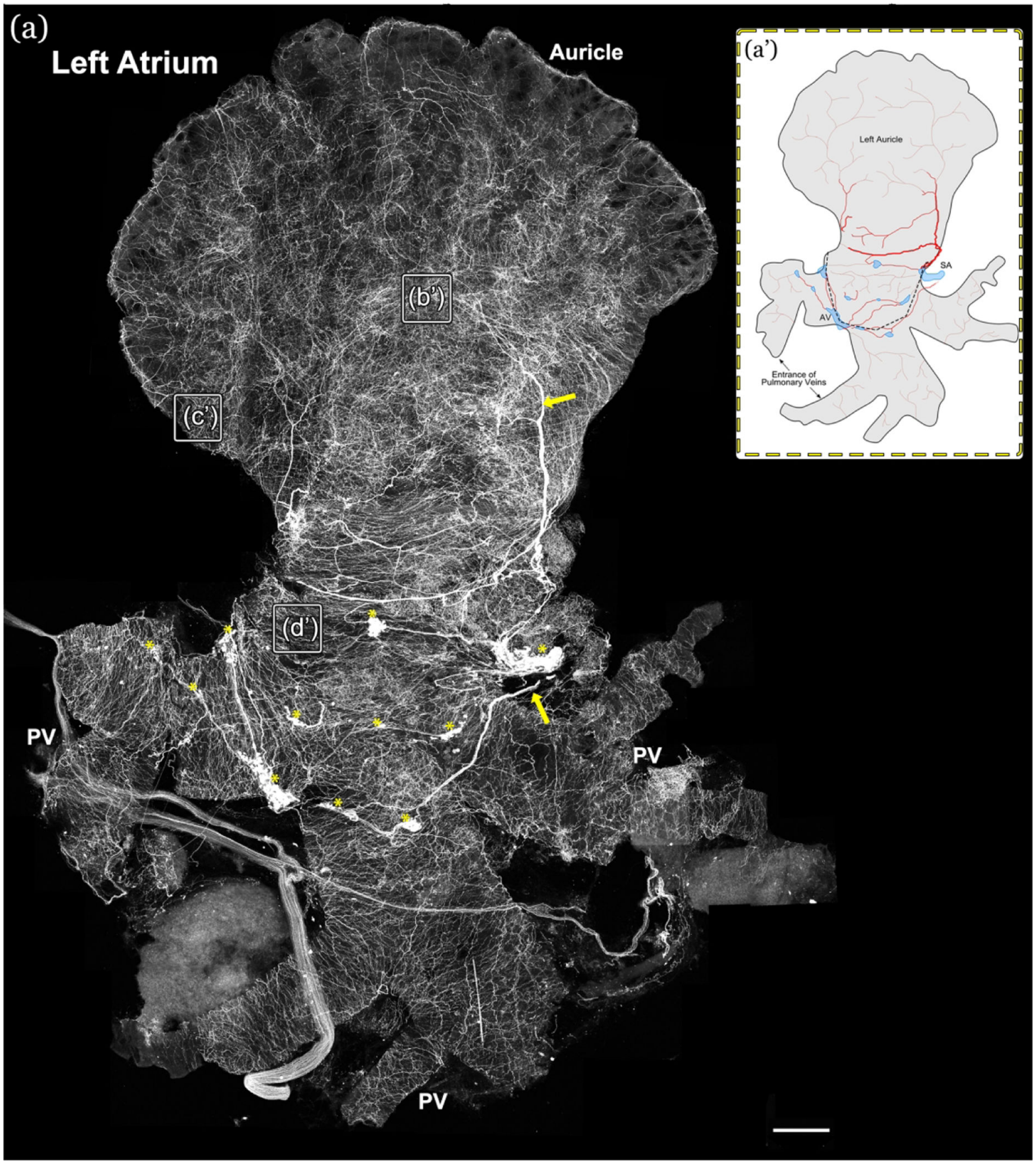

Figure 3.

TH-IR innervation of the whole left atrium flat-mount

(a) A montage of a few hundred all-in-focus maximum confocal projection images shows catecholaminergic (TH-IR) axon innervation of the LA at single cell/axon/varicosity resolution. TH-IR axons entered the LA with large axon bundles (yellow arrows), passed though the ICG (yellow asterisks) and branched out to innervate the entire atrium (see the Figure 7 at a higher magnification). **(a')** Schematic diagram to designate primary features of LA TH-IR axon innervation. Large bundles of TH-IR axons (thick red lines) which bifurcated into smaller bundles (thin red lines) and ultimately innervated the atria with long, varicose, single axon terminals. Ganglia (blue regions), some of which were cut in the process of separating the left and right atria. Boxed regions (**b’**, **c’**, and **d’)** are enlarged and displayed in (Figure 4 b’, c’, and d’, respectively). *LA: left atrium, ICG: intrinsic cardiac ganglia, PV: pulmonary vein.* Scale bar: 500μm.

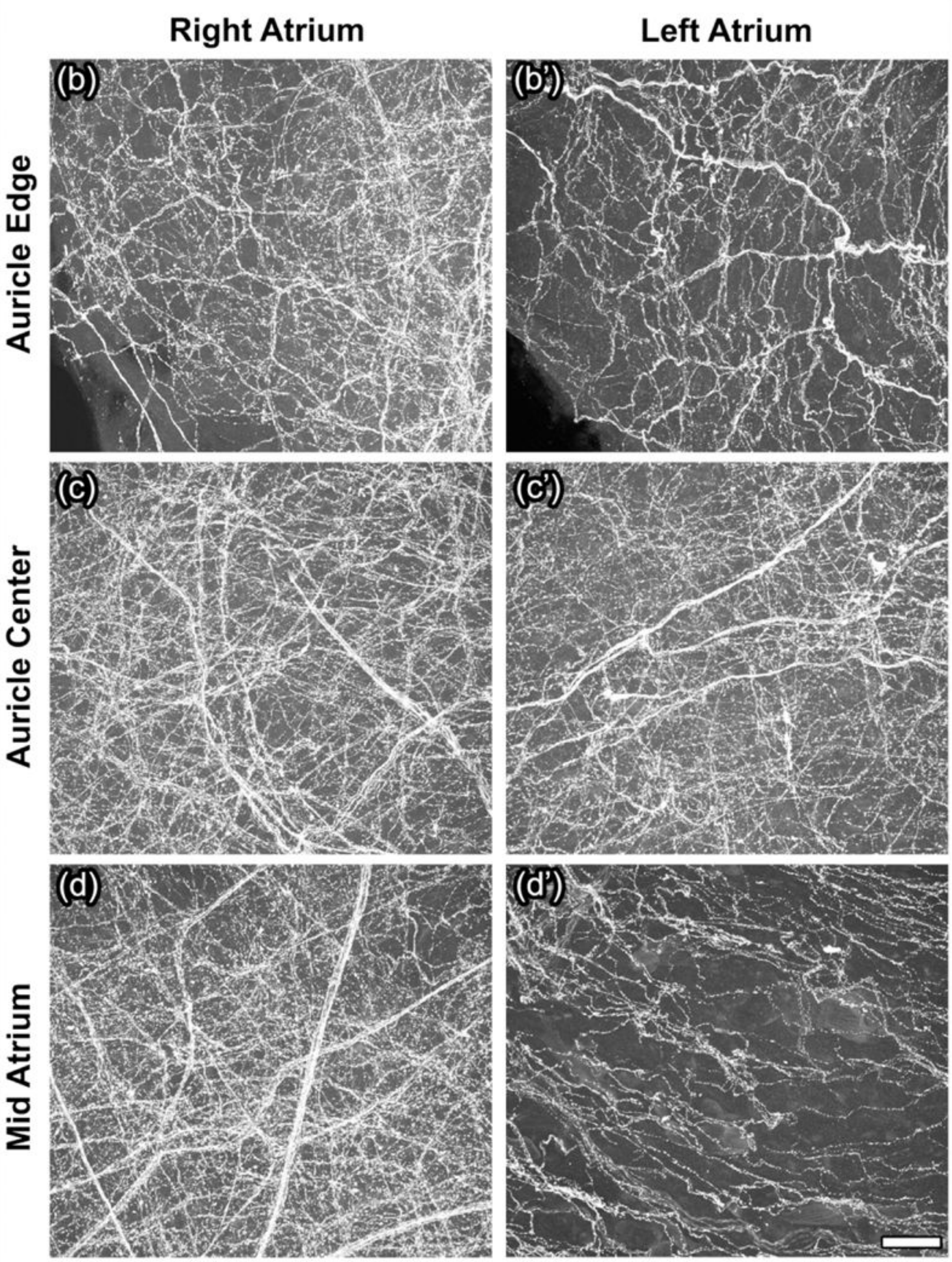

Figure 4.

TH-IR axons in the atrial wall

TH-IR axons heavily innervated all regions in both atria. All-in-focus maximum confocal projections (60–75 optical sections with step size of 0.5μm) of selected regions in the RA and LA. **(b,b')** The edge of the RAu and LAu from the boxed regions of Figures 2 and 3. **b,b'**. The center of the auricle from the region **b and b'** of figures 2 and 3. **(c,c')**. The middle of the atrium from the region **(d and d')** in Figures 2 and 3. *RA: right atrium, LA: left atrium; RAu: right auricle; LAu: Left auricle.* Scale bar: 50μm

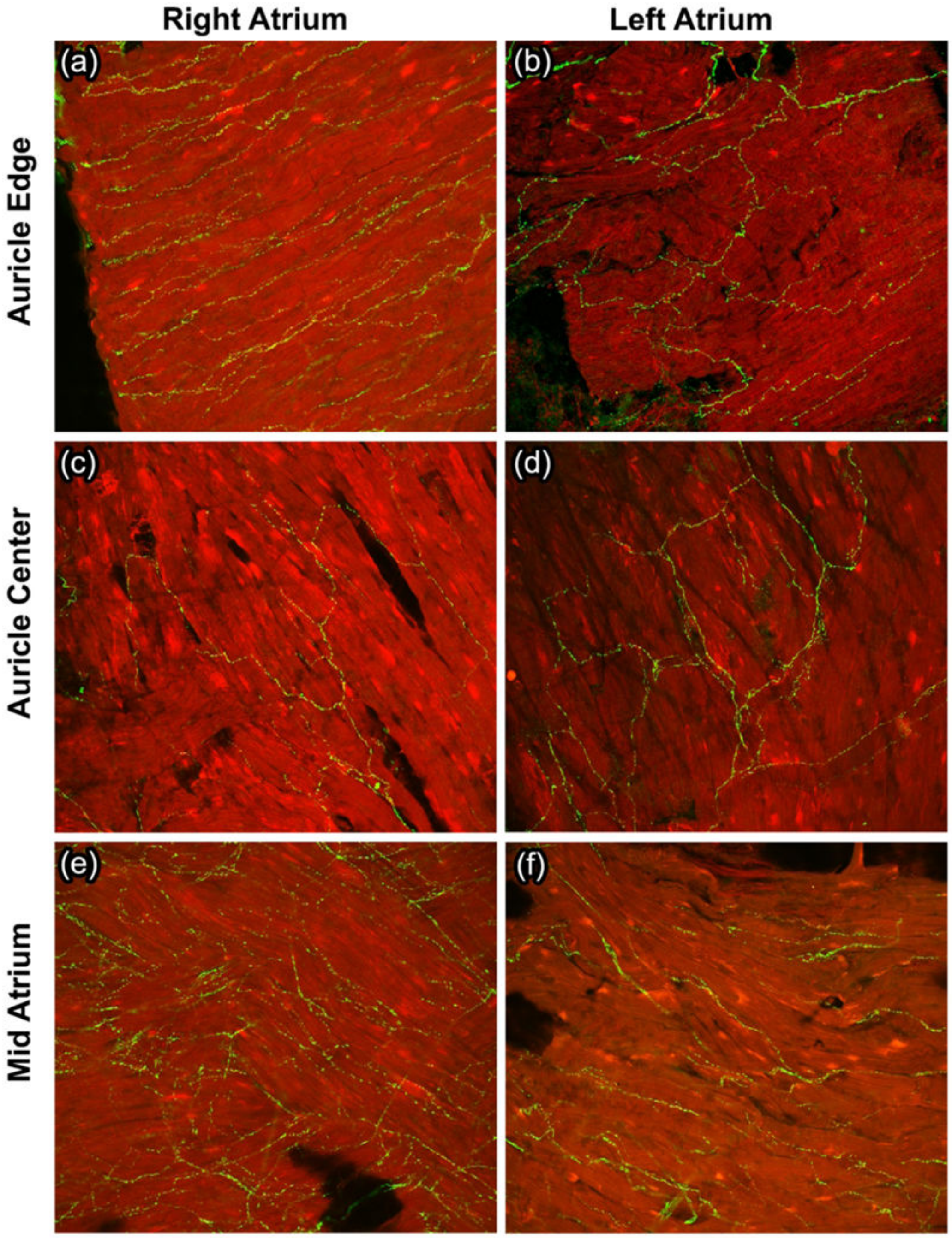

Figure 5.

TH-IR axons in the atrial myocardium

Single confocal optical sections of representative regions of the RA and LA. **(a,b).** The edge of the RAu and LAu. **(c,d).** The center of the RAu and LAu. **(e,f).** The middle of the RA and LA. **Note:** TH-IR varicose axons made close contacts within the muscle in all these regions. Green: TH-IR; Red: Autofluorescence. *RA: right atrium, LA: left atrium, SVC: superior vena cava, RAu: right atrium auricle, LAu: left atrium auricle.* Scale bar: 25 µm.

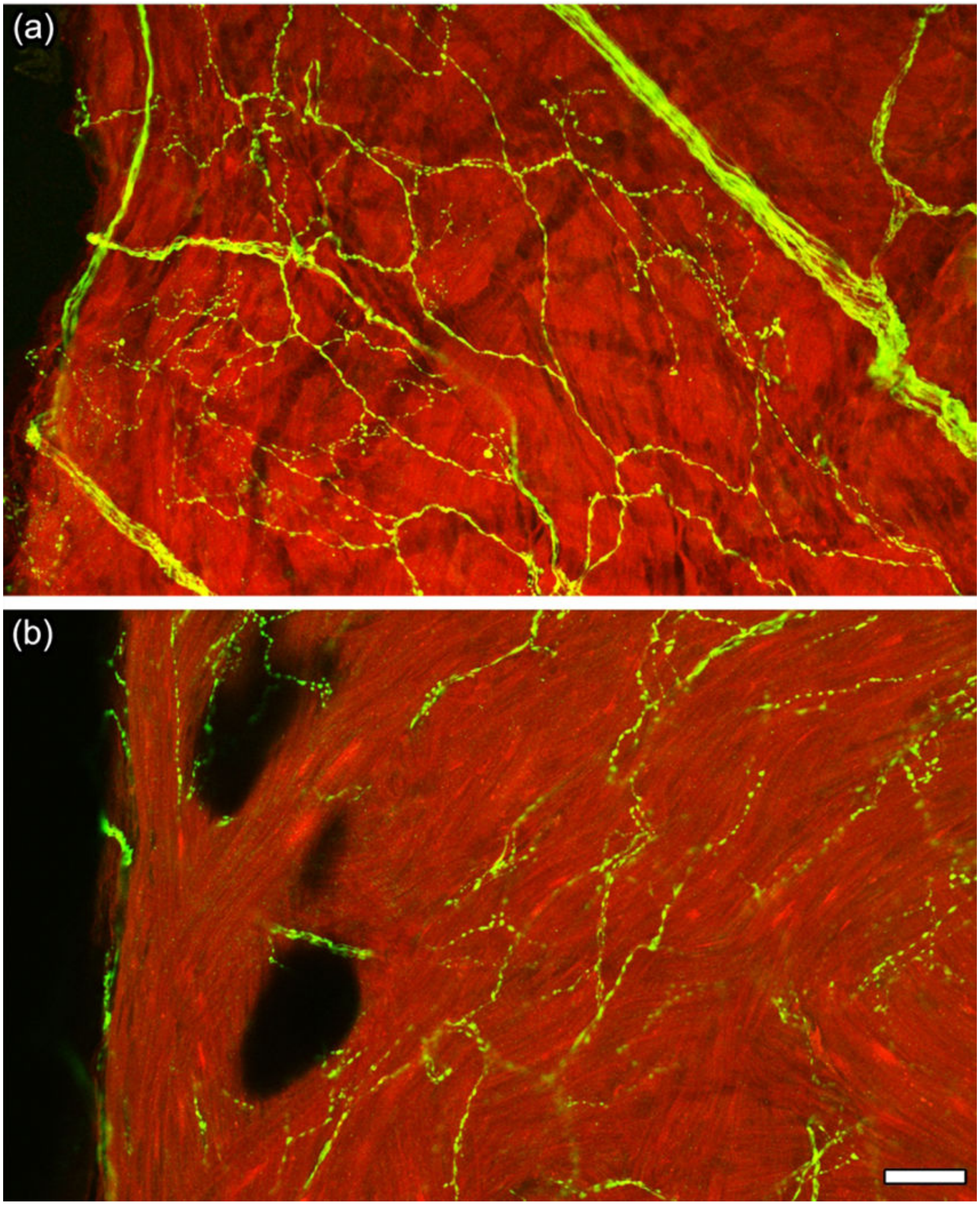

Figure 6.

TH-IR axons in the epicardial and myocardial layers of the auricle

Two confocal optical sections were obtained from the same region near the edge of the left auricle. **(a).** Single optical section contained bundles of TH-IR axons which bifurcated multiple times and formed continuous, long, individual, varicose axons on the epicardium. **(b).** The same region in **Panel (a)** was imaged in the myocardial layer. It showed many fragmentary, short, varicose axons without large bundles. Green: TH-IR; Red: Autofluorescence. Scale bar: 25μm

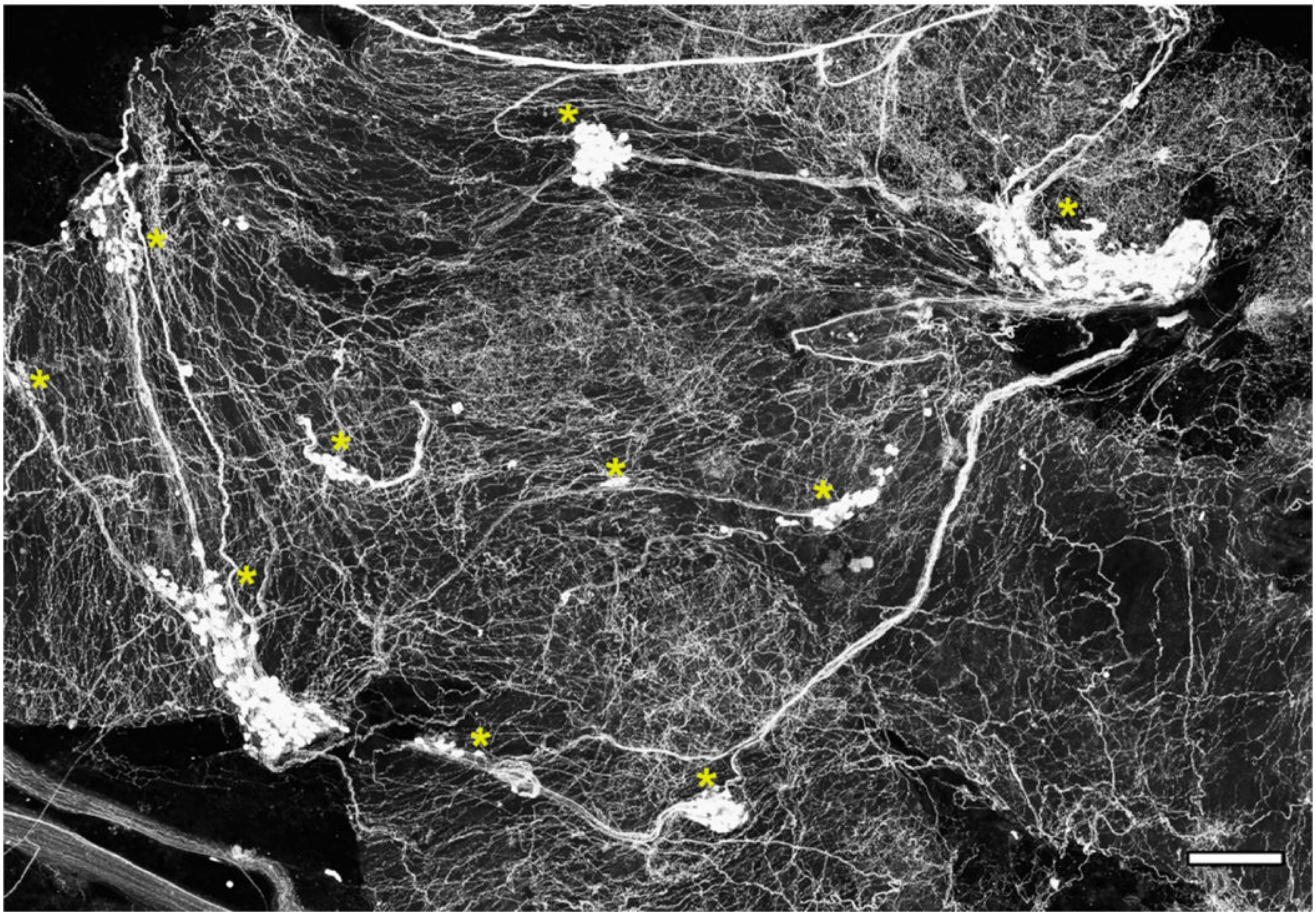

Figure 7.

ICG network

The middle region of the LA from Figure 3 was enlarged to demonstrate the network of ICG (yellow asterisks) on the dorsal surface of the LA. Large bundles of TH-IR axons can be seen traveling among ganglia. Additionally, many neurons in the ICG were TH-IR. Scale bar: 250μm.

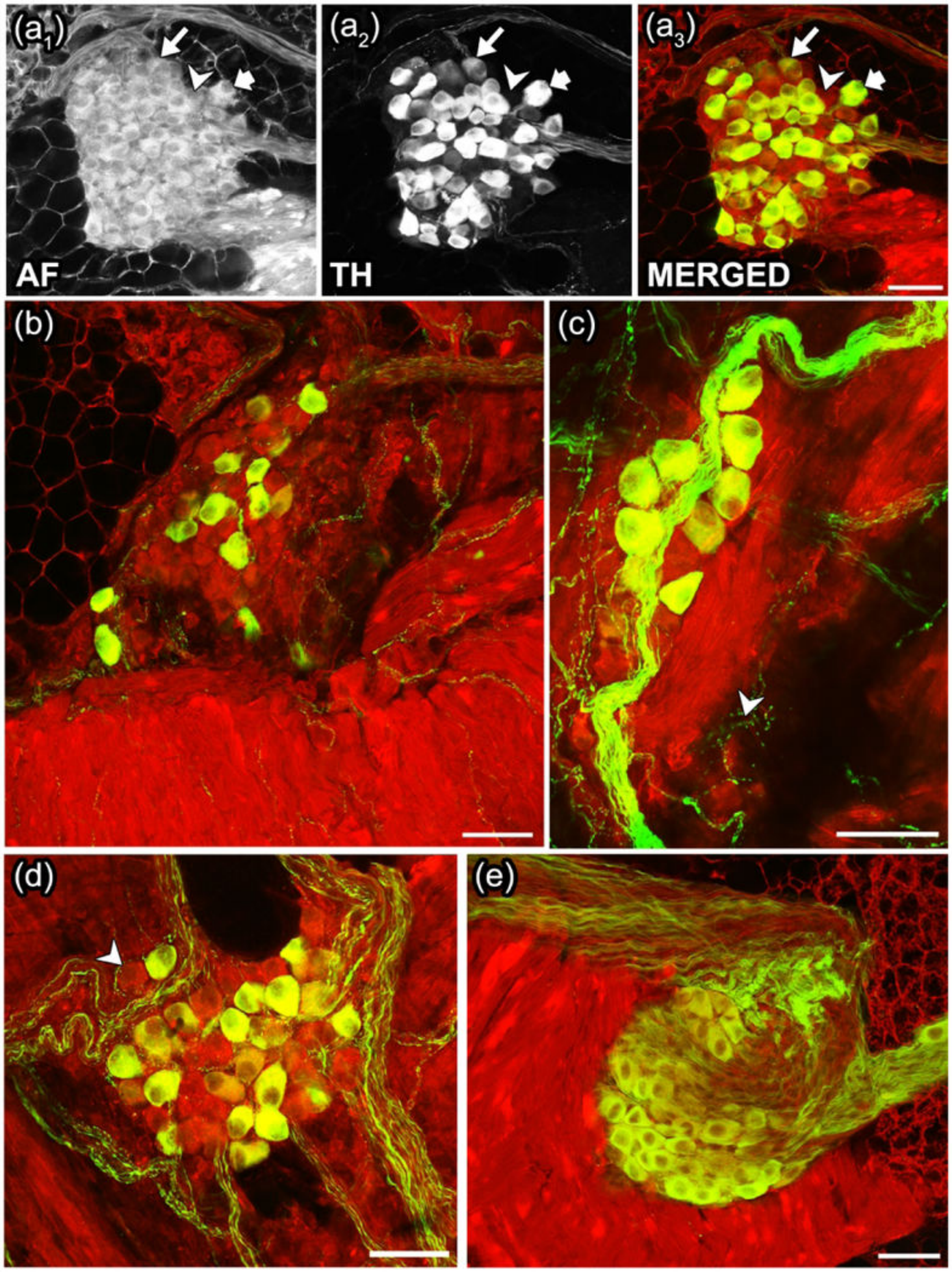

Figure 8.

TH-IR and autofluorescent ICG neurons. **(a).** Autofluorescent ICG neurons (**a**$_1$, gray) were imaged using the 488 nm laser, TH-IR neurons (**a**$_2$, white) were scanned using 543 nm, and the merged image (**a**$_3$) showed the TH-IR neurons (green) and the autofluorescent neurons (red). TH-IR PNs (arrows) could be clearly differentiated from non-TH-IR PNs (arrowheads). Some neurons were strongly TH-IR (short arrows), while the other neurons were weakly labeled (long arrows). Different ICG showed some variation of the amount of TH-IR neurons (**b** vs **a**$_3$). **(c-d).** Bundles of TH-IR axons often traveled through ICG rather than forming varicosities around PNs (arrowheads). **(e).** Sympathetic neurons in an extrinsic ganglion situated near the top of the SVC were mainly TH-IR. *ICG: intrinsic cardiac ganglia, PN: principal neurons, SVC: superior vena cava. White or Green: TH-IR; Gray or Red: Autofluorescence. Scale bar: 50μm*

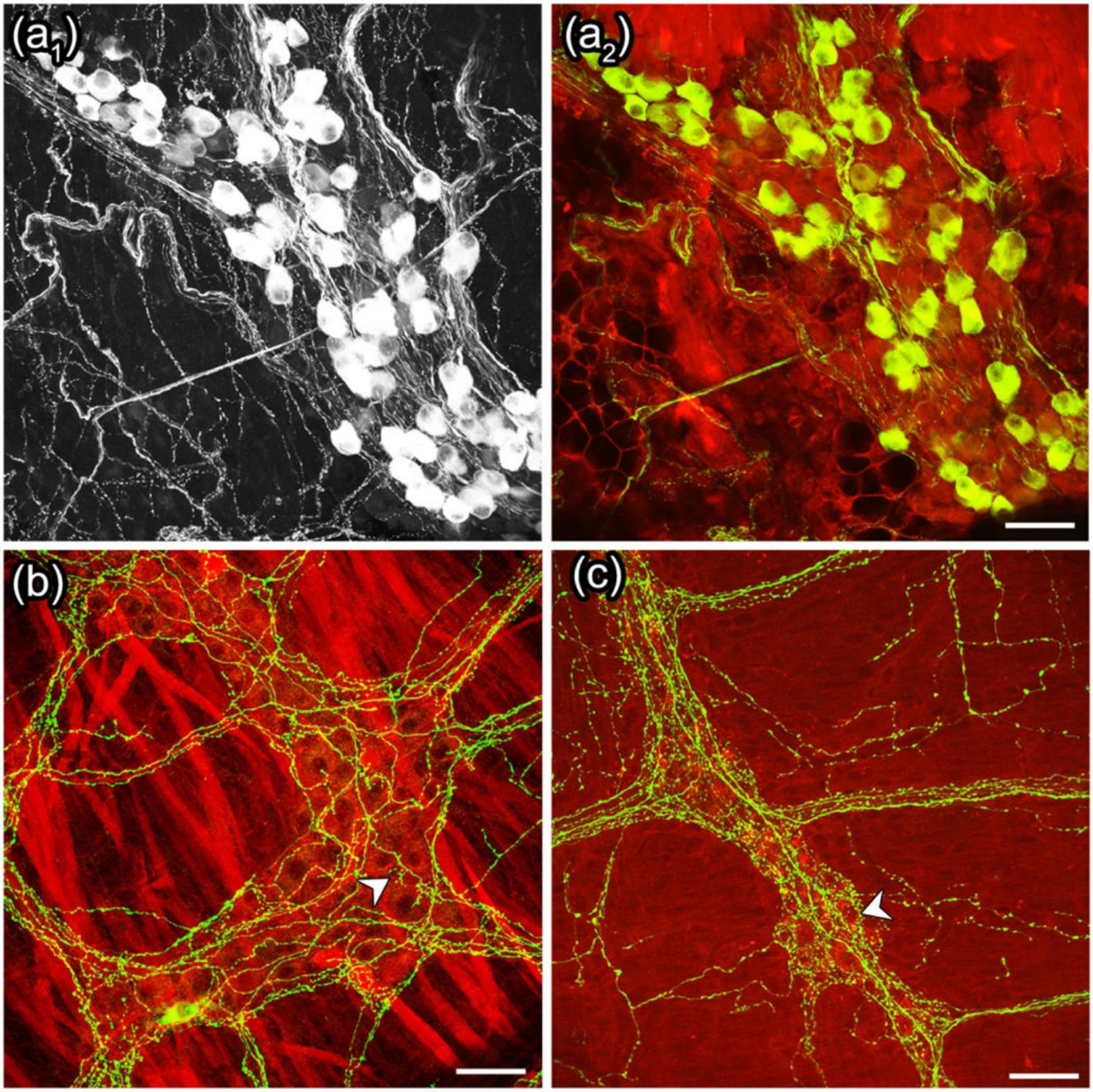

Figure 9.

TH-IR axons in the ICG vs. myenteric ganglia

TH-IR bundles and axons mainly traveled through and between ICG. **(a)**. TH-IR varicosities did not appear to have any direct contacts with any ICG PNs (TH-IR and non-TH-IR) in the maximum confocal projection **(a_1)** and single optical section **(a_2)**. **(b-c).** In contrast to ICG of the heart, TH-IR varicose axons were commonly observed forming synaptic-like terminal endings that tightly encircled individual PNs (arrowheads) in the MG of the stomach (**b**) and small intestine (**c**). *ICG: intrinsic cardiac ganglia, PN: principal neurons. MG:* myenteric ganglia. *Green: TH-IR; Red:* Autofluorescence. Scale bar: 50μm

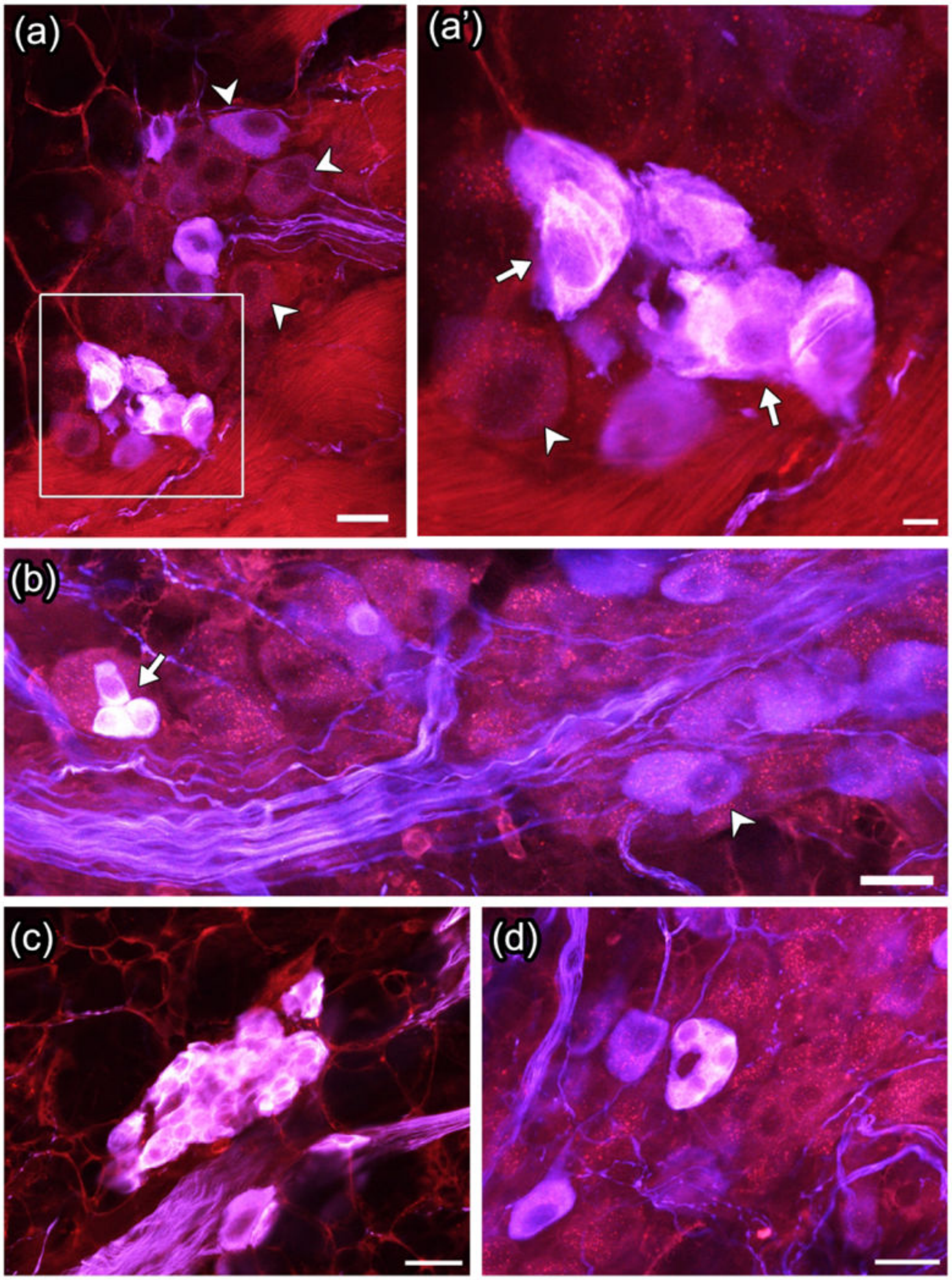

Figure 10.

TH-IR SIF cells in the atria

SIF cells were commonly observed in the RA and LA. **(a-b)**. SIF cells were present adjacent to ICG PNs. The region within the white box in **(a)** was enlarged and represented in **(a')**. SIF cells (arrows) were more strongly TH-IR than ICG PNs (arrowheads) and were smaller in size (< 10 μm in diameter). **(c)**. SIF cells were also commonly observed in large clusters adjacent to large bundles of TH-IR axons. **(d)**. SIF cells were observed in a very close approximation to the ICG. TH-IR axons did not innervate any SIF cells or ICG neurons. *RA:*

right atrium, LA: left atrium, ICG: intrinsic cardiac ganglia, SIF: small intensely fluorescent cells. Purple: TH-IR; White: Strong THIR; Red: Autofluorescence. Scale bar: 20 µm in ***(a,b,c,d)****, and 5 µm in* ***(a')****.*

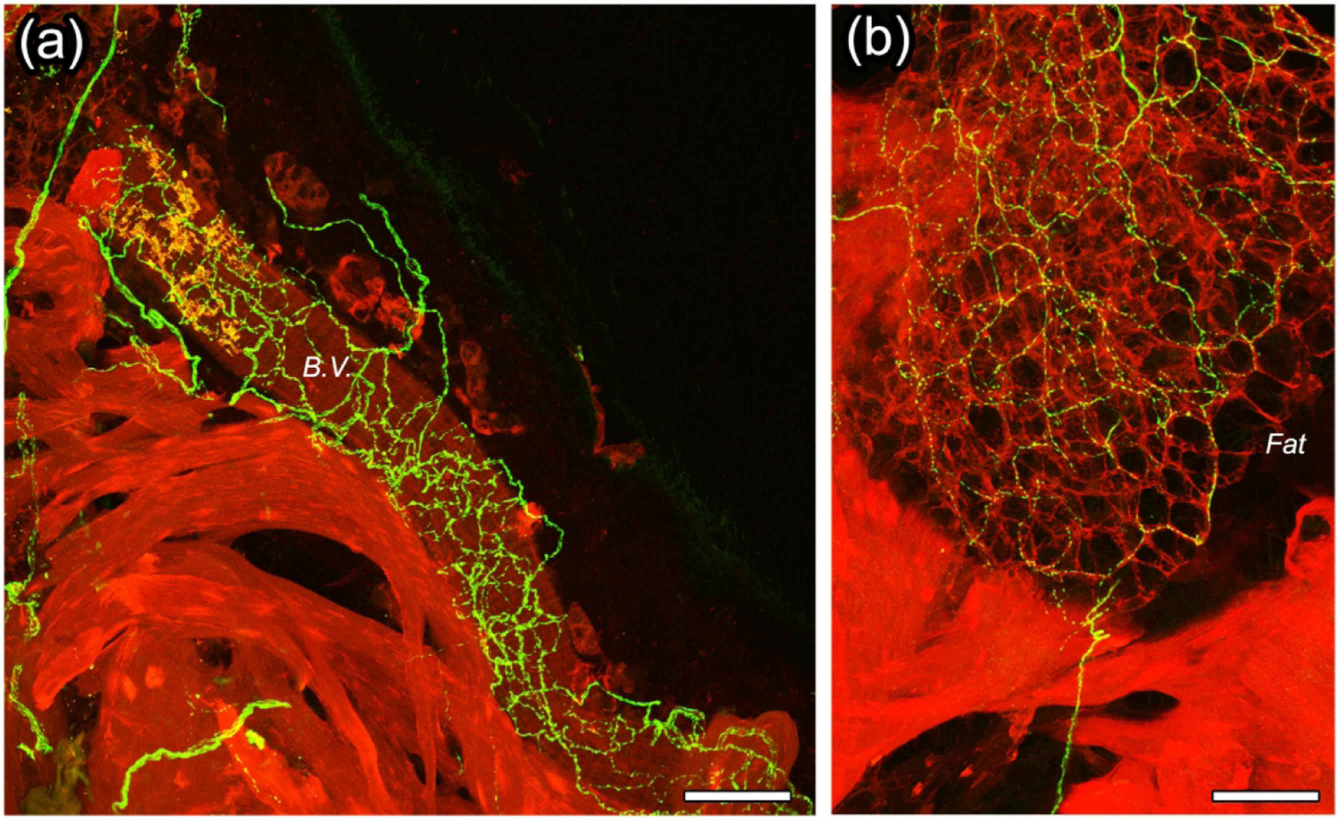

Figure 11.

TH-IR innervation of vasculature and adipocytes in the atria

TH-IR axons innervated the vasculature and adipocytes in and near the atria. **(a).** Numerous TH-IR axons innervated the B.V. by wrapping around the entire length of the structure. **(b).** Fine TH-IR axons ran along the circumference of individual adipocytes. *B.V: blood vessel. Green: TH-IR; Red: Autofluorescence. Scale bar: 50 μm*

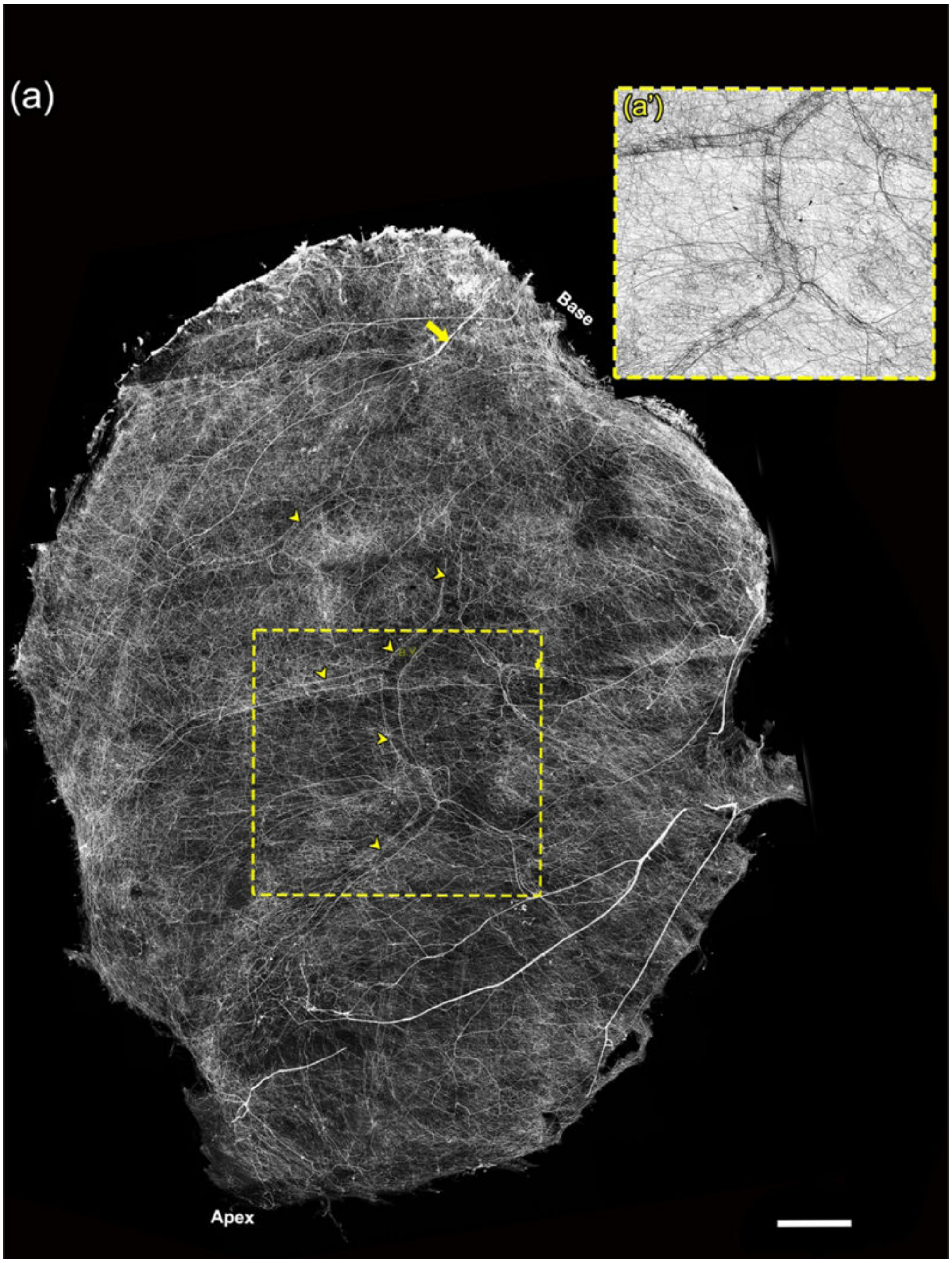

Figure 12.

TH-IR innervation of the flat-mount of RV

(a). A few hundred all-in-focus maximum confocal projections were assembled to form a montage of TH-IR axon innervation of a whole RV flat-mount. Large TH-IR bundles (yellow arrow) entered the RV at the base and branched into smaller bundles that extended towards the apex, and eventually ramified into numerous varicose terminals covering the entire RV. Some of the large TH-IR bundles were cut in the process of dissecting but the majority were intact. There was rich TH-IR axons innervation at the base. **(a')**. Numerous

TH-IR axons were distributed along the vasculature wall or wrapped around them. The vasculature network (yellow arrowheads) was visualized in the RV with a transmural TH-IR axon distribution. *Long yellow arrow: large TH-IR bundle, RV: right ventricle, B.V: blood vessel. Scale bar: 1000 µm*.

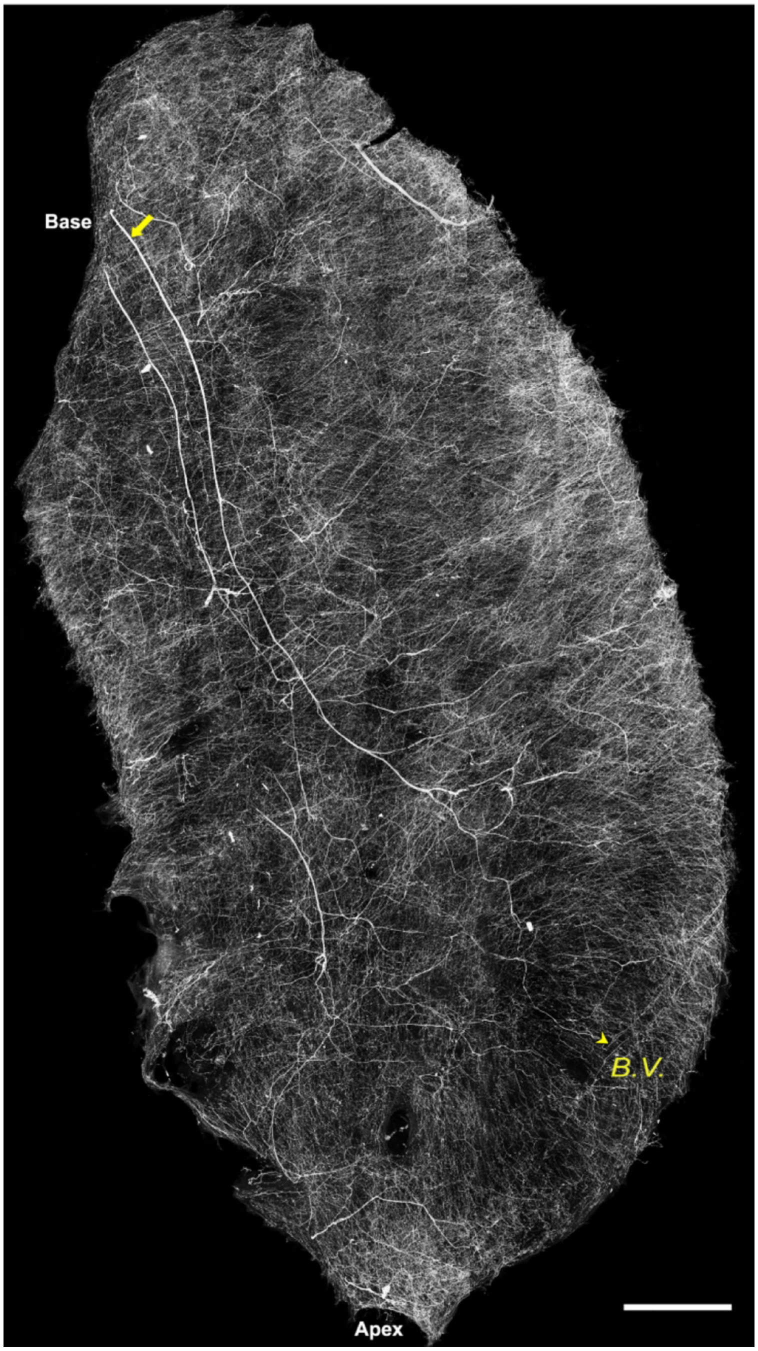

Figure 13.

TH-IR innervation of the flat-mount of LV

A montage of a few hundred all-in-focus maximum confocal projections demonstrating TH-IR axon innervation of the LV at single cell/axon/varicosity resolution. Large TH-IR bundles entered the large partial flat-mount preparation of the LV at the base and ran towards the apex while extending numerous varicose axons that covered the entire LV. The density of TH-IR axon innervation was highest at the base. TH-IR axons were distributed around the B.V. but the visualization of B.V in LV was less apparent than that in R.V due to the greater thickness of tissue and maximal projection could be embedded. Yellow arrow: large TH-IR bundle, B.V: blood vessel, Scale bar: 1000 μm.

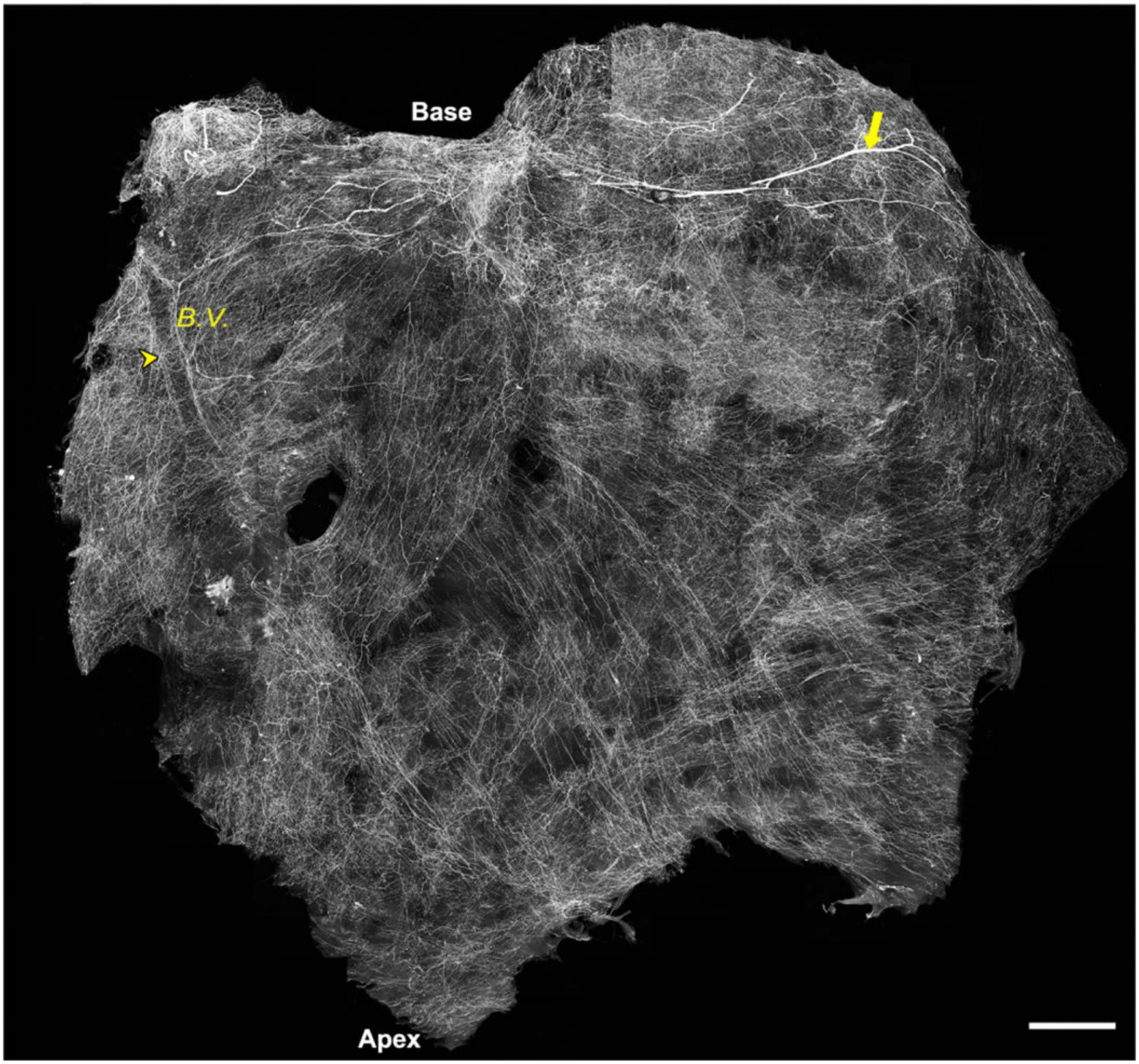

Figure 14.

TH-IR innervation of the flat-mount of IVS

A montage of a few hundred all-in-focus maximum confocal projections demonstrating TH-IR axon innervation of the IVS at single cell/axon/varicosity resolution. Large TH-IR bundles entered the IVS at the base and branched into smaller bundles that formed a very dense TH-IR axon network around the base. Eventually, those axons ramified into numerous varicose terminals covering the entire IVS. The middle and apex regions were less innervated by TH-IR axons relatively compared to the base. A transmural distribution of TH-IR axons was observed along the B.V. *Yellow arrow: large TH-IR bundle, B.V: blood vessel, IVS: interventricular septum. Scale bar: 1000 μm.*

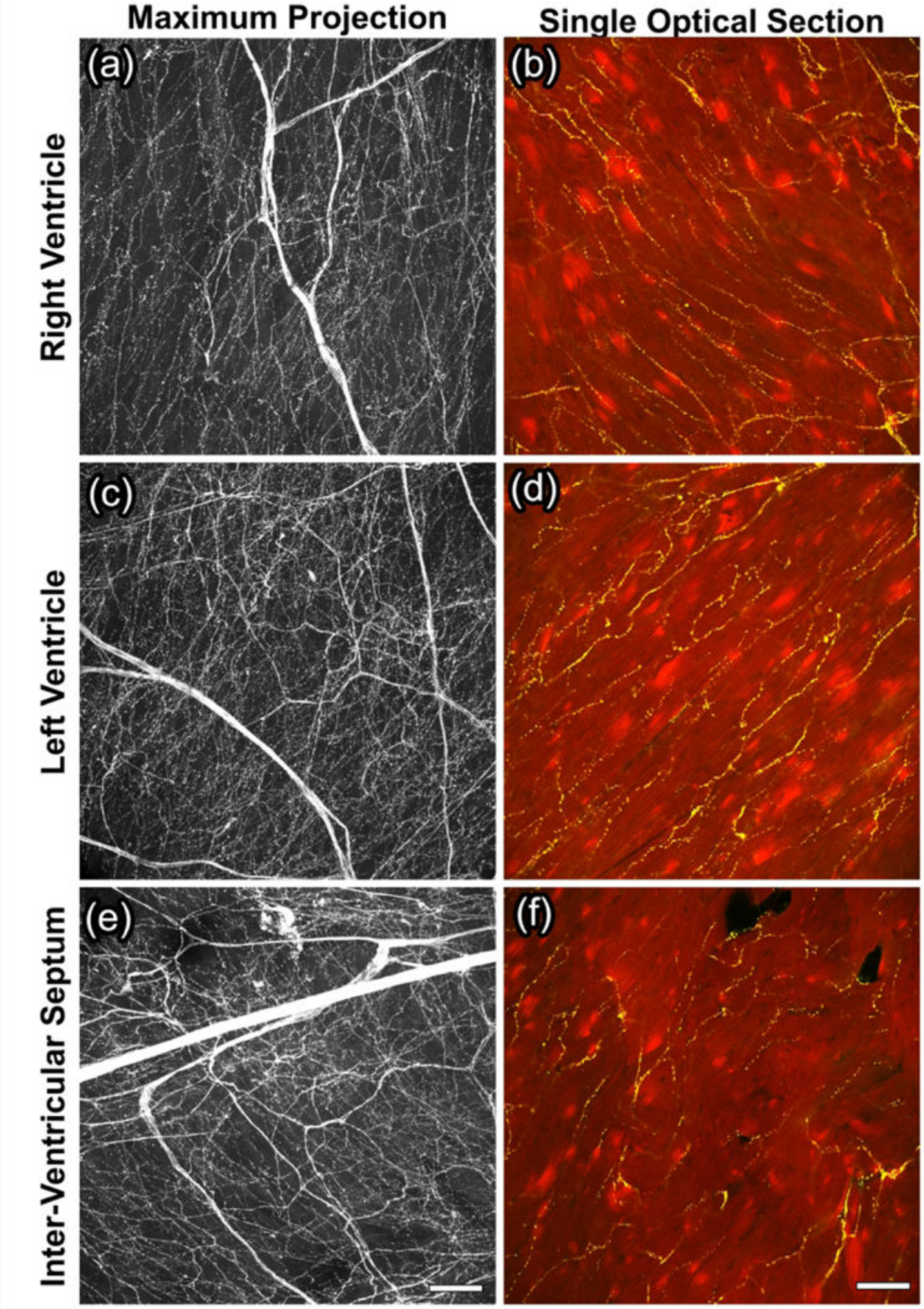

Figure 15.

TH-IR axon innervation of the ventricles

Representative all-in-focus confocal maximum projections (left column) and single optical sections (right column) from randomly-selected regions of the RV, LV, IVS. **(a,c,e)** Large TH-IR bundles bifurcated and projected numerous single, continuous varicose axons in the epicardium layer. **(b,d,f)**. Fragmentary varicose axons are observed in the myocardium of RV, LV, IVS, respectively. This pattern was similar to what was observed in the atria. *RV: right ventricle, LV: left ventricle, IVS: interventricular septum.* Scale bar: 100 µm

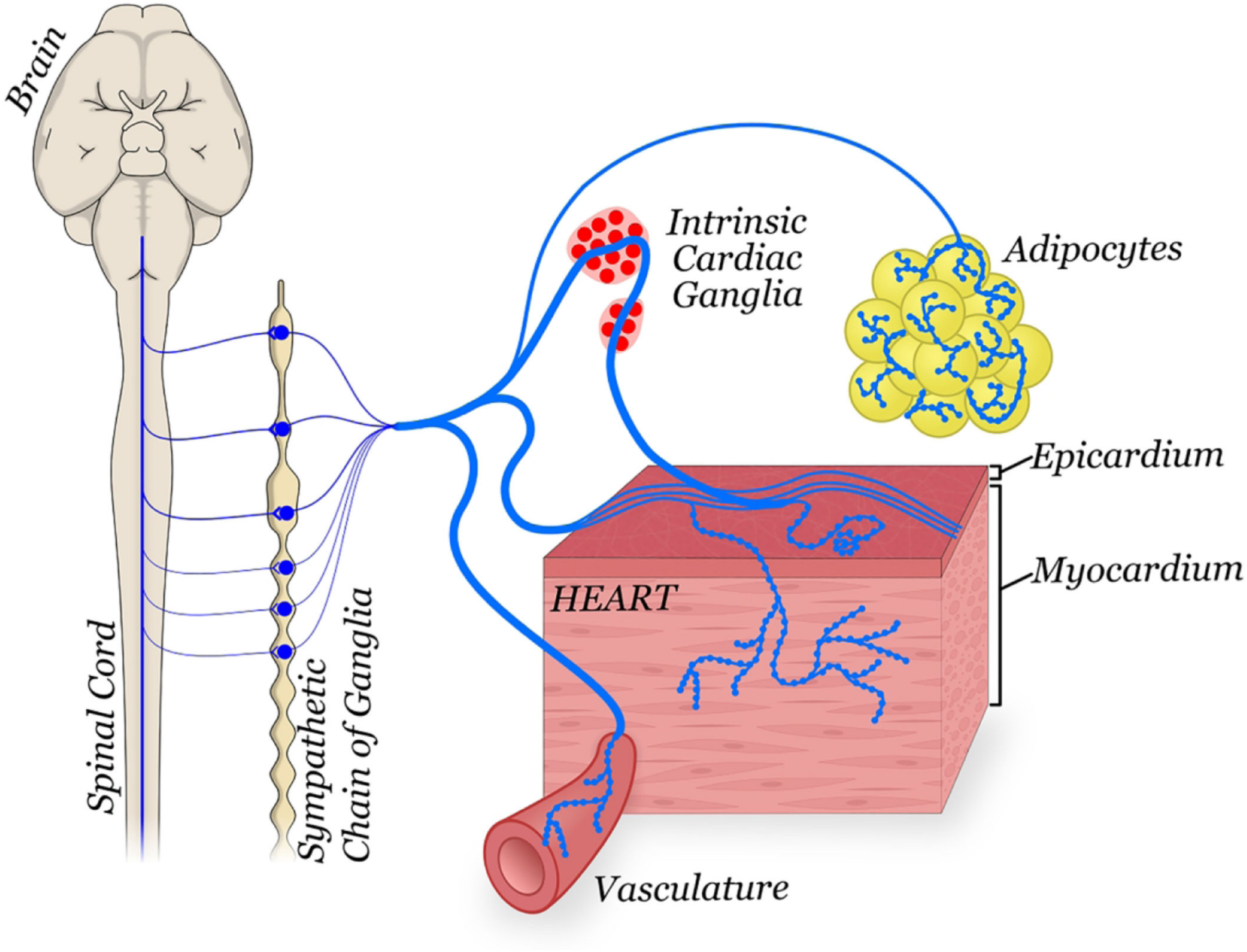

Figure 16.

The overall pattern of TH-IR axon innervation of the heart. This simplified schematic representation showed the general pattern of TH-IR axon innervation in the mouse heart. TH-IR axons, presumably from the sympathetic chain ganglia, entered the heart in large TH-IR bundles which mostly passed through intrinsic cardiac ganglia before innervating their targets (muscles, vasculature, and adipocytes). Other bundles entered the epicardium of the atria and ventricles, bifurcated multiple times, and ultimately formed varicose single-axon innervation that ran deep into the myocardium.

Table 1:

Antibodies used in immunohistochemistry:

Antibody	Concentration	Host	Company	Catalog number	Excitation	RRID
Anti-TH [#]	12 μL/mL	Rabbit	Pel-Freeze	P40101	n/a	AB_461064
Anti-Rabbit [##]	24 μL/mL	Donkey	Invitrogen	A-21207	594 nm	AB_2762827

[#] Primary

[##] Secondary.